JGR Solid Earth

RESEARCH ARTICLE
10.1029/2022JB024008

Hydroacoustic Monitoring of Seafloor Spreading and Transform Faulting in the Equatorial Atlantic Ocean

R. Parnell-Turner[1], D. K. Smith[2], and R. P. Dziak[3]

[1]Scripps Institution of Oceanography, University of California, San Diego, La Jolla, CA, USA, [2]Department of Geology and Geophysics, Woods Hole Oceanographic Institution, Woods Hole, MA, USA, [3]NOAA, Pacific Marine Environmental Laboratory, Newport, OR, USA

Key Points:

- Catalog of 6843 hydroacoustic events recorded by autonomous hydrophones in equatorial Atlantic Ocean between August 2011 and January 2015
- Asymmetric spreading segments have higher hydroacoustic event rate, and frequently host hydrothermal vent systems
- All equatorial Atlantic transforms host aseismic patches, and precursors are common ~2–24 hr before mainshocks of normal faulting events on the ridge axis

Supporting Information:

Supporting Information may be found in the online version of this article.

Correspondence to:

R. Parnell-Turner,
rparnellturner@ucsd.edu

Citation:

Parnell-Turner, R., Smith, D. K., & Dziak, R. P. (2022). Hydroacoustic monitoring of seafloor spreading and transform faulting in the equatorial Atlantic Ocean. *Journal of Geophysical Research: Solid Earth*, *127*, e2022JB024008. https://doi.org/10.1029/2022JB024008

Received 12 JAN 2022
Accepted 16 JUN 2022

Author Contributions:

Conceptualization: R. Parnell-Turner, D. K. Smith, R. P. Dziak
Formal analysis: R. Parnell-Turner, R. P. Dziak
Funding acquisition: D. K. Smith, R. P. Dziak
Investigation: R. P. Dziak
Methodology: R. Parnell-Turner
Project Administration: R. Parnell-Turner, D. K. Smith
Visualization: R. Parnell-Turner
Writing – original draft: R. Parnell-Turner, D. K. Smith

Abstract Seismicity along mid-ocean ridges and oceanic transform faults provides insights into the processes of crustal accretion and strike-slip deformation. In the equatorial Atlantic ocean, the slow-spreading Mid-Atlantic Ridge is offset by some of the longest-offset transform faults on Earth, which remain relatively poorly understood due to its remote location far from land-based teleseismic receivers. A catalog of T-phase events detected by an array of 10 autonomous hydrophones deployed between 2011 and 2015, extending from 20°N to 10°S is presented. The final catalog of 6,843 events has a magnitude of completeness of 3.3, compared to 4.4 for the International Seismic Center teleseismic catalog covering the same region, and allows investigation of the dual processes of crustal accretion and transform fault slip. The seismicity rate observed at asymmetric spreading segments (those hosting detachment faults) is significantly higher than that of symmetric spreading centers, and 74% of known hydrothermal vents along the equatorial Mid-Atlantic Ridge occur on asymmetric spreading segments. Aseismic patches are present on nearly all equatorial Atlantic transform faults, including on the Romanche transform where regional rotation and transpression could explain both bathymetric uplift and reduction in seismic activity. The observed patterns in seismicity provide insight into the thermal and mechanical structure of the ridge axis and associated transform faults, and potentially provide a method for investigating the distribution of hydrothermal vent systems.

Plain Language Summary New oceanic seafloor is created at mid-ocean ridges where tectonic plates move apart, causing seafloor volcanism and deep-sea hydrothermal venting. Meanwhile, changes in the direction of plate motion occur along strike-slip faults which can be hundreds of kilometers long, called oceanic transforms, and offset the mid-ocean ridge. Neither of these processes are fully understood, but constantly generate numerous small earthquakes which in places like the remote equatorial Atlantic Ocean, often go undetected by far-away instruments on land. Using a network of hydrophones spaced thousands of kilometers apart and moored ~800 m below the sea surface, over 6,000 earthquakes in the equatorial Atlantic ocean were located from 2011 to 2015, roughly 10 times more than would have been detected by land-based stations alone. Similar to previous studies, we find that transform faults have patches where very few earthquakes occur and hence may be locked or creeping, likely due to spatial variability in the thermal properties of the lithosphere and underlying mantle. More earthquakes occurred in places where the plates spread apart asymmetrically, and hydrothermal vents are also more likely to occur in places where spreading is asymmetric.

1. Introduction

A significant fraction of Earth's surface is formed as the lithospheric plates move apart at a relatively slow pace (<35 mm yr^{-1}), accounting for seafloor in most of the Atlantic, Indian, and Arctic oceans. In these slow-spreading settings, crust is thought to form in a variety of styles, which result in a spectrum ranging between magma-rich segments producing abyssal hill topography, to melt-poor end-members where mantle-derived rocks are brought to the surface by kilometer-scale detachment faults (e.g., Cannet et al., 1995, 1997; Dick et al., 2003). Under slow-spreading conditions, the relative roles of faulting and dike injection control the formation of new oceanic crust, leading to a system that is highly sensitive to changes in magma supply and resulting in the distinct modes of accretion (Escartin et al., 2008; Olive et al., 2010; Smith et al., 2008; Tucholke et al., 1998). The modes of accretion are in turn reflected in the thermal structure, magma supply, and hydrothermal circulation at the axis (Escartin et al., 2008). Abyssal hill terrain forms by symmetric accretion, dominated by magmatism and short-lived high-angle faulting on both flanks, also found at fast-spreading ridges such as the East Pacific Rise. Studies to date indicate that spreading segments dominated by abyssal hill topography have lower overall levels

Writing – review & editing: R. Parnell-Turner, D. K. Smith, R. P. Dziak

of seismicity, which is mostly restricted to segment ends (e.g., Escartin et al., 2008; Smith et al., 2002). Detachment terrain forms by asymmetrical accretion involving an active detachment fault along one ridge flank and is associated with higher levels of near-continuous seismicity (Escartin et al., 2008; Smith et al., 2008).

Strike-slip motion on oceanic transform faults (OTFs) plays a fundamental role in seafloor spreading, by offsetting adjacent mid-ocean ridge segments, and allowing the plates to move apart while new crust is formed (e.g., Oldenburg & Brune, 1972; Sykes, 1967; Wilson, 1965). Under slow-spreading conditions, such as those found on the Mid-Atlantic Ridge (MAR), transform faults coincide with zones of weakened lithosphere, leaving behind deep fracture zone traces with crust thinned relative to adjacent spreading segments (Blackman & Forsyth, 1991; Gregg et al., 2007; Kuo & Forsyth, 1988).

Studies of earthquake seismicity on OTFs have revealed that most have large seismic moment deficits, leading to the conclusion that displacement must instead be accommodated by aseismic creep (e.g., Boettcher & Jordan, 2004; Brune, 1968; Wolfson-Schwehr & Boettcher, 2018). Earthquakes on OTFs are surprisingly small with highly variable seismic coupling along strike, and rupture often occurs in patches separated by zones of lower coupling that host microearthquakes or creep (e.g., Boettcher & Jordan, 2004). Local earthquake monitoring experiments have made progress on understanding these issues on individual OTFs (e.g., Aderhold & Abercrombie, 2016; Braunmiller & Nábělek, 2008; McGuire et al., 2012); however, such efforts are few and sparsely distributed. Scaling relation analysis shows that about 85% of the slip above the 600°C isotherm must be accommodated by aseismic creep and is not dependent upon OTF length or slip rate (Boettcher & Jordan, 2004). Hence, it is now thought that both seismic and subseismic mechanisms, such as steady aseismic creep, silent earthquakes, and infraseismic (quiet) events, could play an important role in accommodating fault motion (Boettcher & Jordan, 2004). A recent global study of relocated earthquakes on 138 OTFs found that creeping segments account for 64% of the OTF length (Shi et al., 2021) and could explain why OTFs generate fewer earthquakes than expected. This study was, however, restricted to teleseismically detected earthquakes with $M_w > 5$, and hence, questions remain about the possibility smaller-magnitude events on creeping patches.

Despite the importance of crustal accretion under slow-spreading conditions and the central role of OTFs, direct observations remain challenging due to difficulties in accessing the deep oceans. Earthquake monitoring provides a simple method to tackle this problem, since both the motion on oceanic transform faults, and the tectono-magmatic process of crustal accretion, give rise to seismicity. Teleseismic earthquake catalogs are now able to reliably locate earthquakes along the entire global mid-ocean ridge (MOR) system. However, since they rely on arrivals detected by the mostly land-based global seismograph network, smaller events ($M_w < 4.5$) in remote ocean basins are not routinely located. Temporary ocean bottom seismograph (OBS) networks are able to overcome this problem for localized studies (e.g., Braunmiller & Nábělek, 2008; Gong et al., 2022), but logistical and cost challenges mean that such experiments are rarely able to capture segment- or transform-scale variations in seismicity. Hydroacoustically detected earthquakes, located using T-phases recorded by sparse networks of autonomous hydrophones, are able to bridge this gap between global and local earthquake catalogs (e.g., Fox et al., 1995; Johnson, 1966). The modest costs, the capability of detecting smaller magnitude events, and high location accuracy of hydrophones provide a means to understand crustal accretion and seismicity on transform faults over thousands of kilometers, using arrays of only several instruments (e.g., Bohnenstiehl et al., 2003; Dziak et al., 2004; Fox et al., 2001; Smith et al., 2003).

In an earlier experiment, six autonomous hydrophones moored in the North Atlantic (15°–35°N) recorded the seismicity of the slow-spreading MAR for 4 years (Smith et al., 2002). The improved detection capability and earthquake location accuracy of the hydrophone array compared to teleseismic networks provided new insights into the overall spatial and temporal patterns in ridge axis tectonic and magmatic processes (Bohnenstiehl & Kleinrock, 2000, 2003; Dziak et al., 2004; Escartin et al., 2003, 2008; Simão et al., 2010). In order to continue to expand our knowledge of slow-spreading mid-ocean ridges, we deployed a hydrophone array in the equatorial Atlantic between August 2011 and January 2015 (Figure 1). The MAR in the equatorial Atlantic Ocean spreads at rates of 30 ± 2 mm yr^{-1} (Demets & Merkouriev, 2019). This region is interesting because of its tectonic history associated with the opening of the Atlantic Ocean (Bonatti, 1996; Jones, 1987; Klitgord & Schouten, 1986; Le Pichon & Fox, 1971; Uchupi, 1989). Here, a strongly segmented MAR is offset by some of the longest OTFs in the oceans (e.g., >900 km Romanche transform). Offsets are especially large between about 3°N and 3°S, where the cumulative length of the transforms is longer than the cumulative length of the ridge axis (Bonatti et al., 1994). Here, we use T-phase arrivals detected by this network of autonomous hydrophones in the equatorial

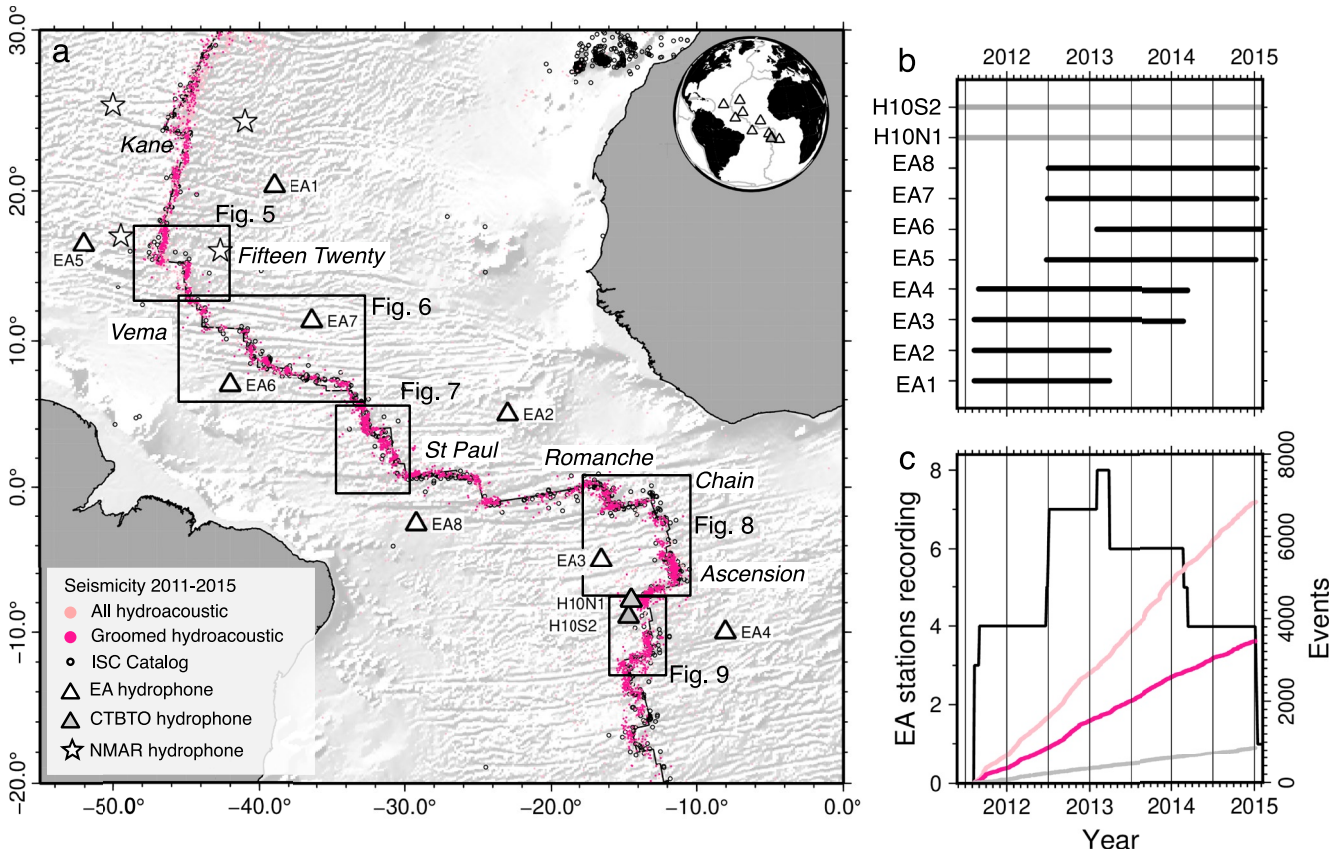

Figure 1. (a) Bathymetry and seismicity in equatorial Atlantic Ocean (bathymetric data from Ryan et al., 2009). Pink dots are hydroacoustic T-phase origins from 2011 to 2015 (this study); black circles are teleseismic events from International Seismological Center (ISC) catalog from 2011 to 2015; white/gray triangles are hydrophones from EA and CTBTO networks, respectively; stars are NMAR array (Smith et al., 2003). (b) Bars are recording periods for hydrophones used to detect T-phases. (c) Time series of recording network, and event count. Black line is number of EA hydrophones recording; light/dark pink lines are total/groomed hydroacoustic events, respectively; gray line is number of teleseismic events (ISC catalog).

Atlantic to understand variations in crustal accretion style, transform fault seismicity, and hydrothermal vent distribution at this less well known section of the MAR.

2. Hydroacoustic Data

A network of moored autonomous PMEL/NOAA hydrophones was deployed between 2011 and 2015 at ~1,000 km spacing around the MAR in the equatorial Atlantic Ocean (Figure 1), spanning from 20°N to 10°S. Each instrument was placed within the acoustic low-velocity zone known as the Sound Fixing and Ranging (SOFAR) channel (approximately 800 m below the sea surface), and data were recorded between 10 August 2011 and 13 January 2015, yielding 1,252 days (3 years and 5 months) of monitoring. Instrument deployment and recovery schedules meant that the number of hydrophones simultaneously recording varied during the experiment, with all eight instruments operating for only 1 month in 2013. Waveform data were recorded at 16-bit resolution and a sampling rate of 250 Hz; further instrumentation details are given in Dziak et al. (2004). In order to improve spatial and temporal coverage, data from hydroacoustic station HA10 (Ascension Island) were also used, which is operated by the Comprehensive Nuclear-Test-Ban Treaty Organization (CTBTO) and records data at the sampling rate of 250 Hz (Okal, 2001). Station HA10 consists of two hydrophone triplets, arranged as a pair of arrays of three hydrophones on an equilateral triangle with ~2 km separation, located to the north and south of Ascension Island. For this study, waveform data recorded by two hydrophones (HA10S2 and HA10N1) were used, which were both continuously recording while the PMEL/NOAA moored hydrophone network was operating.

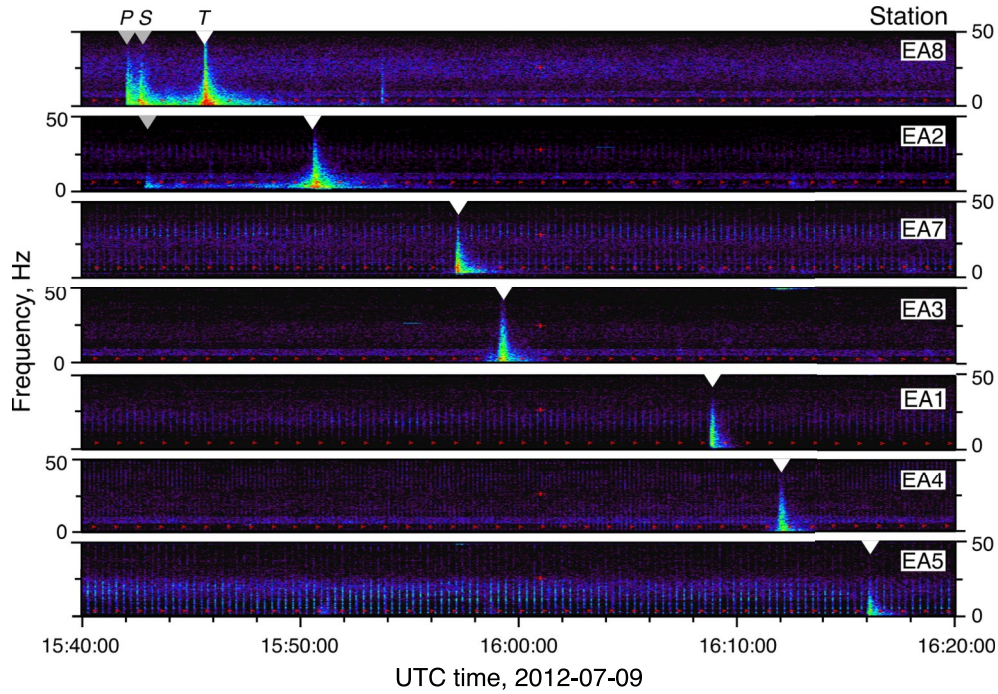

Figure 2. Example spectra from M_w 4.8 event located on St Paul transform fault (29.125°W 0.819°N), recorded across EA network on 9 July 2012, International Seismological Center (ISC) catalog origin time 15:40:21 UTC. Labeled gray triangles on EA8 spectrogram are P- and S-arrivals, P-arrival also visible on EA2; white triangles are T-arrivals recorded on all stations; arrivals in 5–25 Hz frequency band spaced at 20 s intervals seen on EA2, EA7, EA1, EA4 and EA5 are likely airgun shots associated with exploration activity on west African margin.

2.1. T-Phase Source Location and Analysis

Waveforms from all available stations were used to estimate T-phase source locations and magnitude estimates, although it is currently not feasible to obtain source mechanism and hypocentral depth estimates from such hydroacoustic data. Acoustic waveforms from each hydrophone were decomposed into time versus frequency spectrograms, which were then used to visually identify T-phase arrivals across the network simultaneously (Figure 2). T-phase arrivals, corresponding to the peak energy at each station, were picked by a single analyst for the entire observation period. Arrivals from each event were tracked across all recording instruments, and the move-out pattern was used to associate phases from multiple events that passed through the network at the same time. In addition to seismic T-phases, we were also able to visually distinguish other noise sources, including marine mammals and man-made sources such as airguns and vessel traffic.

T-phase origin location, source time, and their respective errors were calculated for events with three or more arrival picks, using an iterative, nonlinear least squares method (details given in Fox et al., 2001; Slack et al., 1999), with ocean acoustic velocities from the Generalized Digital Environmental Model (Teague et al., 1990). Location errors within the equatorial Atlantic network are based on point-source simulations calibrated using known sound sources (Fox et al., 2001) and modified for use in the Atlantic ocean with an arrival time picking error (1 σ) of 1.5 s (Smith et al., 2003). Median errors in latitude and longitude at the 68% confidence level are ∼8 km within the network, and rise to >30 km outside of the network (Figure 3). Spatial variability in error estimates of the final catalog is due to changes in network geometry over time, as instruments were deployed and recovered piece-wise (Figure 1b). The resulting hydroacoustic catalog contains 6,843 events. In order to examine seismicity patterns in more detail, we defined a groomed hydroacoustic catalog (n = 3,458), consisting of events with latitude and longitude location uncertainty <0.5°, detected by four or more stations, and located within 200 km of the ridge axis or OTF. An estimate of the acoustic magnitude, or source level (*SL*), is used as a proxy for earthquake magnitude. *SL* represents the acoustic energy of the earthquake at the seafloor-water interface, measured in units of decibels (dB) relative to pressure (μPa) at a reference distance of 1 m above the seafloor, and normalized by

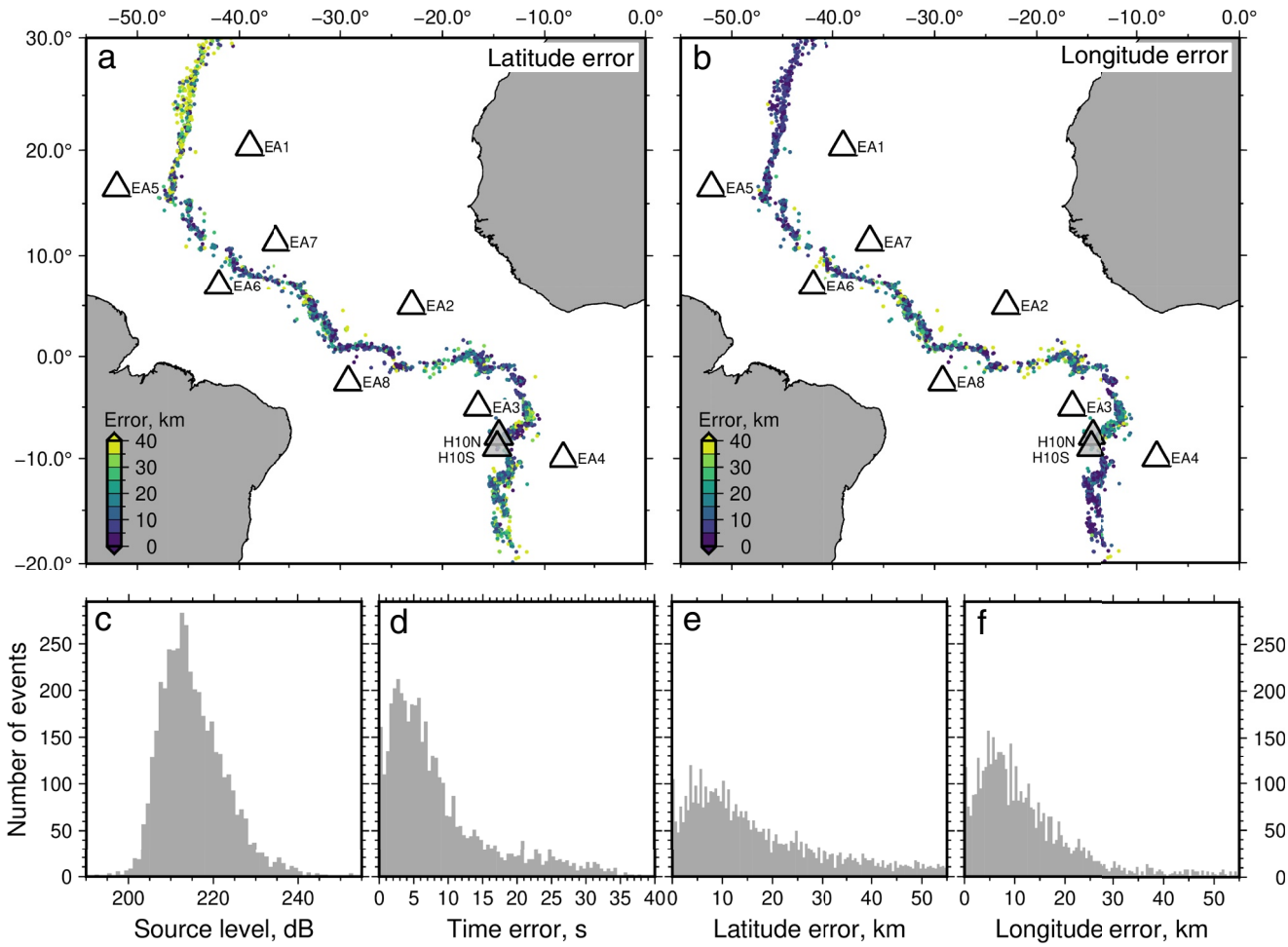

Figure 3. T-phase origin uncertainty estimates for entire hydroacoustic catalog (n = 6,843). (a) and (b) T-phase origins, colored by error in latitude and longitude, respectively. (c)–(f) Histograms showing source level, origin time error, latitude error, and longitude error, respectively.

sampling rate to yield spectral density; that is, dB relative to μPa/$\sqrt{Hz}$ at 1 m (Dziak, 2001; Dziak et al., 1997; Fox et al., 2001). The *SL* for each event was determined by averaging independent station *SL* estimates, accounting for hydrophone instrument response, and for transmission loss during propagation. We assume a spherical transmission loss model (r^{-2}) between the seafloor and the SOFAR channel and then cylindrical spreading (r^{-1}) for the portion of the T-phase path within the SOFAR channel (Smith et al., 2003). Although this approach to transmission loss is adequate for the purposes of the relative and catalog-scale analysis we pursue here (e.g., Bohnenstiehl et al., 2002; Williams et al., 2006), without a detailed transmission loss model, acoustic magnitudes of individual events are considered to be preliminary.

2.2. Completeness and Magnitude Estimates

In order to explore the resulting T-phase catalog, we first need to determine the completeness level, that is, the source level above which the data set is complete, analogous to magnitude of completeness, M_{Wc}. For this purpose, we compare the hydroacoustic catalog to the reviewed International Seismological Center (ISC) Bulletin from 1970 to 2015 (International Seismological Centre, 2022), with all magnitudes converted to moment magnitudes (M_w) using the empirical relation of Das et al. (2011). We assume that earthquakes follow a Gutenberg–Richter relationship of the form

$$\log_{10}\left(N_{\geq M_{Wc}}\right) = A - b\,(M_W)\,, \tag{1}$$

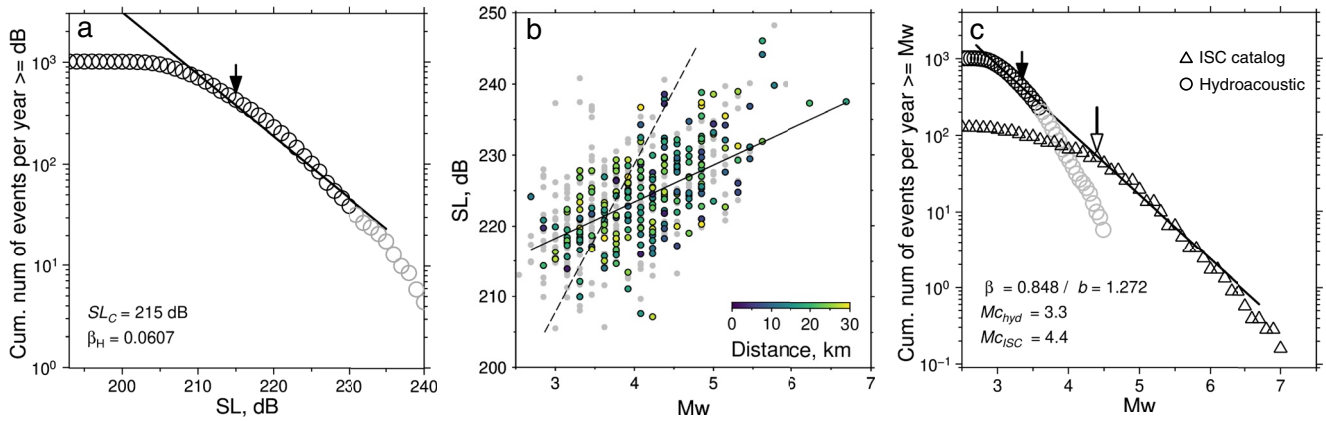

Figure 4. (a) Source level (SL)-frequency distribution of hydroacoustic catalog in 1 dB bins, for events detected by >3 stations (10 August 2011 to 6 January 2015), normalized per year. Hydroacoustic SL-frequency distribution is described by $\log_{10}(N_{\geq SL}) = A_h - b_h SL$, where b_h is estimated using the maximum likelihood method (e.g., Aki, 1965), and SL of completeness (SL_c, black arrow) is obtained at 90% confidence level following Wiemer and Wyss (2000), giving a value of 215 dB (b) Source level and M_w for events identified in both hydroacoustic and International Seismological Center (ISC) catalogs, colored by distance between their respective origin locations. Dashed line is linear regression (Pan & Dziewonski, 2005); solid line is affine mapping method following (Olive & Escartin, 2016). (c) Frequency-magnitude distribution (FMD) for hydroacoustic and ISC catalogs, mapped from source level to M_w using affine mapping method. For ISC catalog, β and M_{cISC} (4.4) obtained using maximum likelihood method (Kanamori, 1983). Resulting magnitude of completeness for the T-phase catalog, Mc_{hyd}, is 3.3.

where $N_{\geq M_{Wc}}$ is the frequency of earthquakes greater than a given magnitude of completeness, M_{Wc}, A is a parameter related to the seismicity rate, and b is the slope of the Gutenberg-Richter distribution. Similarly, the source level of completeness, SL_C, can be written as

$$\log_{10}(N_{\geq SL}) = A_h - b_h(SL) \tag{2}$$

where $N_{>SL}$ is the number of events greater than a given SL, A_h is a constant dependent on the seismicity rate, and b_h is the slope of the distribution, which can be estimated using the maximum likelihood method (Aki, 1965; Frohlich & Davis, 1993). M_{Wc} and SL_C were obtained by determining values of A, A_h, b, and b_h for increasingly large trial values of M_{Wc} and SL, which were then used to generate synthetic power law (SL-frequency) distributions (Wiemer & Wyss, 2000). We calculated the goodness of fit between each synthetic power law fit to the data and the observed frequency-magnitude distribution, and defined M_{Wc} and SL_C as the levels at which 90% of the data can be modeled by a power law fit. After excluding events with $SL > 230$ dB to account for clipping of the hydrophone sensors during the largest events, we obtain a SL_C estimate of 215 dB, and a M_{Wc} for the ISC catalog of 4.4 (Figure 4).

The physical mechanisms responsible for excitation of T-phases are not yet fully understood. The T-phase amplitude recorded at any given hydrophone station depends upon source parameters, seismic-to-acoustic conversion at the seafloor, mode of acoustic propagation, and the receiver (de Groot-Hedlin & Orcutt, 2001; Dziak, 2001; Okal, 2008). The relationship between SL and the amount of energy released during an earthquake remains uncertain, and several attempts have been made to describe the relationship (Bohnenstiehl et al., 2003; Dziak et al., 1997; Pan & Dziewonski, 2005; Yang & Forsyth, 2003). One simple approach is to compare the M_w and SL of event pairs found in both teleseismic and hydroacoustic catalogs (Pan & Dziewonski, 2005). For this comparison, we identified pairs by seeking events with origin times <60 s apart, and with locations less than 30 km apart. During the time window of the EA experiment (10 August 2011 to 13 January 2015), there are 698 events in the ISC catalog within 500 km of the MAR and inside the EA network (defined as extending from the Kane transform in the north to the Bode Verde transform in the south). Of these events, 556 (~80%) can be identified in the hydroacoustic catalog based upon our 60 s matching criteria. This detection rate is, however, an underestimate since events in the ISC catalog are located using an effectively static network of stations, whereas the EA catalog is constructed from events recorded by a frequently changing array (see Figure 1). Station coverage and spacing varied considerably during the EA experimental time window, meaning that some events in the ISC catalog are likely to have been undetected by the hydrophone network.

A least-square linear fit was calculated between the M_w and SL for event pairs, with weightings of 100, 10, and 1 given to events that were 10, 20, and 30 km apart, respectively (Figure 4b). The resulting fit predicts an

unrealistically low magnitude of completeness (<200 dB) for the hydroacoustic catalog, reflecting the gaps in our understanding of T-phase excitation, and hence, this method is not likely to be appropriate (Figure 4b). Since the *SL*-frequency distribution closely resembles the Gutenberg-Richter power law, *SL* can be used as a relative proxy for moment magnitude, M_0, using the distribution of magnitudes in the teleseismic catalog (e.g., Olive & Escartin, 2016). We assume the transformation between M_0 and *SL* can be expressed as

$$SL = p_1 \log_{10}(M_0) + p_2 \tag{3}$$

where the parameter p_1 is evaluated using

$$p_1 = \frac{\beta}{\beta_h}, \tag{4}$$

where $\beta = 2/3b$, yielding $p_1 = 13.97$. The parameter p_2 is a scaling factor for the distribution of hydroacoustic source levels, proportional to the duration-corrected moment release rate of the teleseismic ISC catalog (Frohlich, 2007). Adjusting the 56 years timespan of the ISC catalog to the 5.1 year duration of the hydroacoustic

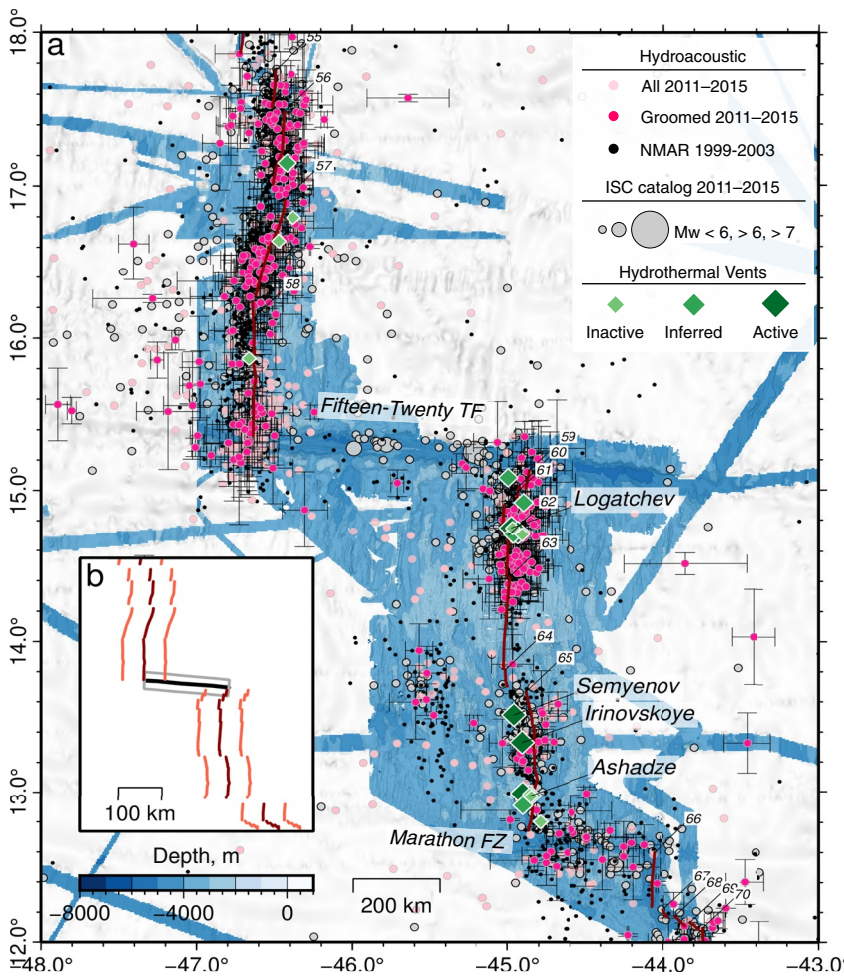

Figure 5. (a) Bathymetry, seismicity and venting along MAR 12°–18°N (bathymetric data from Ryan et al., 2009). Pink dots are hydroacoustic events 2011–2015, with 1σ error bars for groomed catalog (this study); black dots are hydroacoustic events 1999–2003 (Smith et al., 2003); gray circles are ISC catalog 2011–2015 scaled by M_w; green diamonds are hydrothermal vents (Beaulieu & Szafrański, 2020); dark red lines mark spreading ridge segments, labels on northern end. (b) Inset showing example ridge segment and transform fault interpretation (dark red and black lines, respectively). Orange/gray polygons are 50/20 km either side of ridge/transform, respectively, used to select associated events; distances chosen to account for orientation of ridges and transforms with respect to hydrophone network, leading to differences in location uncertainty.

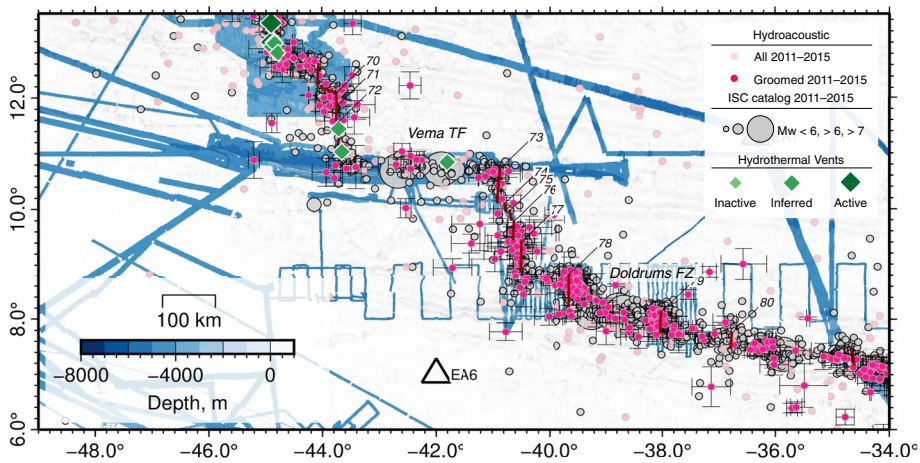

Figure 6. Bathymetry, seismicity and venting along MAR 6°–12.5°N (bathyetric data from Ryan et al., 2009). Pink dots are hydroacoustic events 2011–2015, with 1σ error bars for groomed catalog (this study); gray circles are ISC catalog 2011–2015 scaled by M_w; green diamonds are hydrothermal vents (Beaulieu & Szafrański, 2020); dark red lines mark spreading ridge segments, labels on northern end.

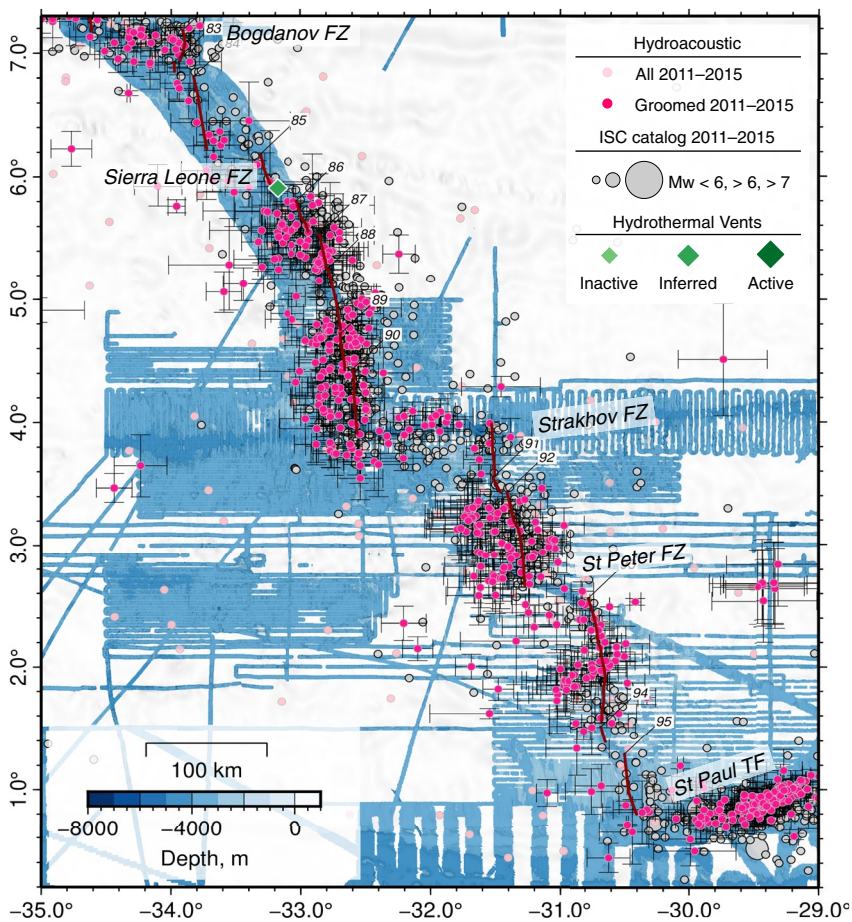

Figure 7. Bathymetry, seismicity and venting along MAR 0°–7°N (bathymetric data from Ryan et al., 2009). Pink dots are hydroacoustic events 2011–2015, with 1σ error bars for groomed catalog (this study); gray circles are ISC catalog 2011–2015 scaled by M_w; green diamonds are hydrothermal vents (Beaulieu & Szafrański, 2020); dark red lines mark spreading ridge segments, labels on northern end.

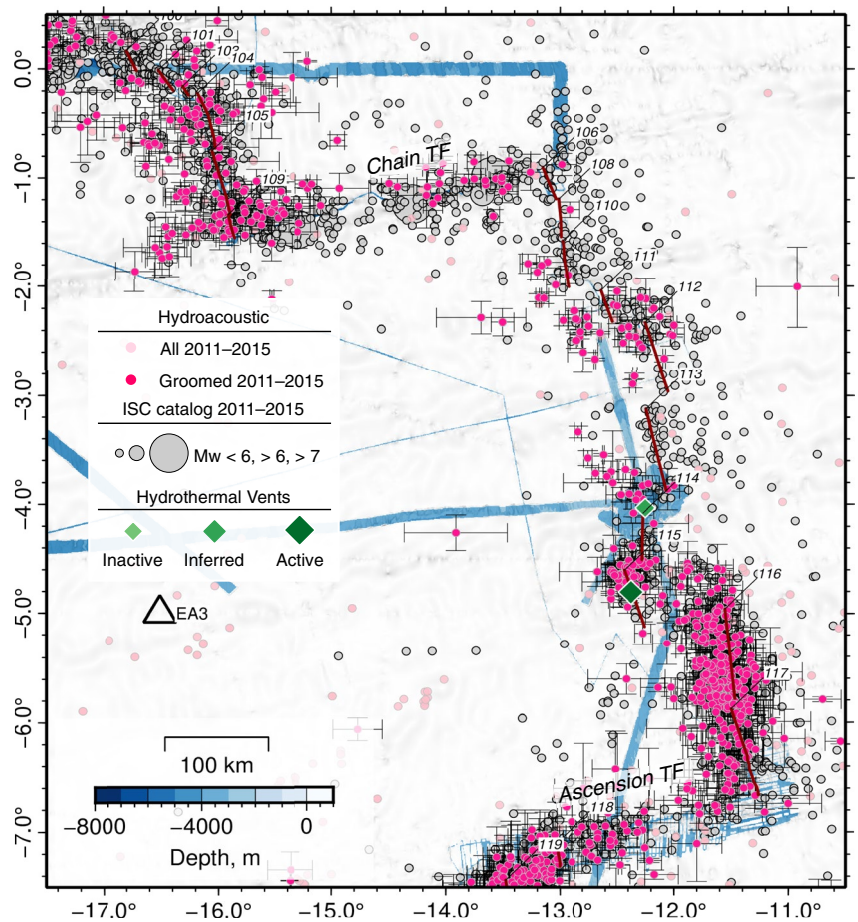

Figure 8. Bathymetry, seismicity and venting along MAR 0°–7°S (bathymetric data from Ryan et al., 2009). Pink dots are hydroacoustic events 2011–2015, with 1σ error bars for groomed catalog (this study); gray circles are ISC catalog 2011–2015 scaled by M_w; green diamonds are hydrothermal vents (Beaulieu & Szafrański, 2020); dark red lines mark spreading ridge segments, labels on northern end.

catalog, we are able to match the moment release rate from the ISC catalog to the hydroacoustic catalog, with $p_2 = 18.5$. The resulting function (solid line, Figure 4b) shows a reasonable fit to matched events from both ISC and hydroacoustic catalogs and is consistent with our estimate of SL_c of 215 dB, which translates to a magnitude of completion (Mc_{hyd}) of 3.3 for the hydroacoustic catalog. While this conversion from acoustic source level to magnitude is imperfect, for the purposes of this study it does provide a useful qualitative indicator of relative seismicity between spreading segments and transforms.

3. Results and Discussion

3.1. Segment-Scale Variations in Seismicity

Hydroacoustic event locations correspond to where seismic energy radiates from the seafloor into the water column, and hence may not exactly correspond to earthquake epicenters (e.g., Talandier & Okal, 1998; Williams et al., 2006). Hence, interpretations of kilometer-scale variations in seismicity patterns are necessarily tentative, and we focus our interpretation on segment-scale seismicity, and relative variations in the distribution of hydrophone-recorded events.

Overlap in coverage between the EA experiment presented here and an earlier T-phase experiment on the northern MAR (NMAR; Smith et al., 2003) from 1999 to 2003 (Figure 1) provides the opportunity for comparison near the Fifteen twenty transform fault (Figure 5). T-phase origins from both studies are in good agreement, with notable seismicity in the segments immediately to the north and south of the Fifteen twenty transform fault.

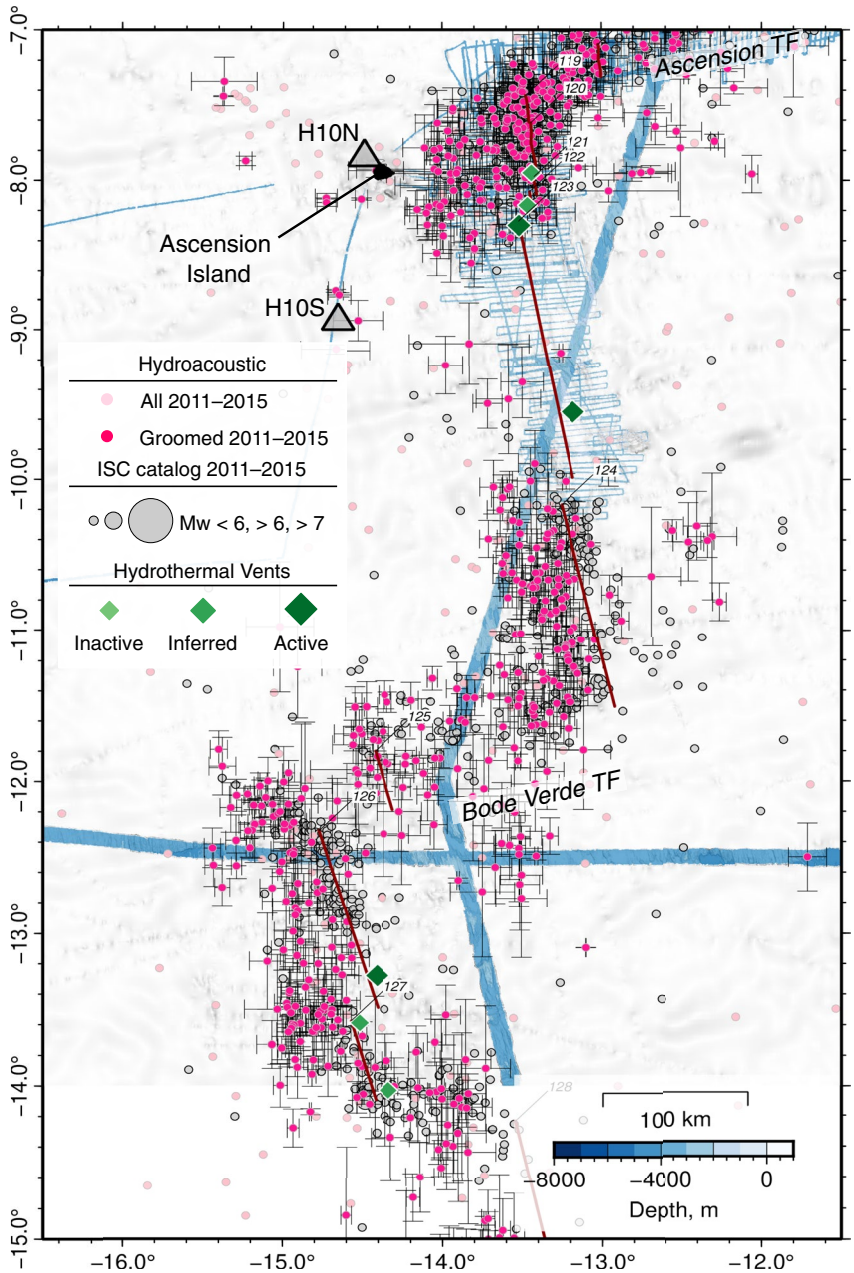

Figure 9. Bathymetry, seismicity and venting along MAR 7°–13°S (bathymetric data from Ryan et al., 2009). Pink dots are hydroacoustic events 2011–2015, with 1σ error bars for groomed catalog (this study); gray circles are ISC catalog 2011–2015 scaled by M_w; green diamonds are hydrothermal vents (Beaulieu & Szafrański, 2020); dark red lines mark spreading ridge segments, labels on northern end.

A notable reduction in seismicity is evident in both hydroacoustic catalogs and the ISC catalog between 13.7°N and 14.4°N (segment 64 and the southern portion of segment 63; Figure 5), attributed to higher magma supply relative to adjacent segments, where detachment-style spreading dominates (Smith et al., 2003, 2006). Anomalous seismicity located ~70 km west of the axis is also evident in all three catalogs, previously suggested to be due to a ridge jump and incipient rifting, or due to stresses arising from the presence of a North America-South America-Africa plate triple junction in the area (Escartin et al., 2003).

Figures 6–9 show hydroacoustic origins covering selected spreading segments of the MAR from the Vema fracture zone at 11°N to near the Bode Verde fracture zone at 14°S. Spreading segments with relatively few

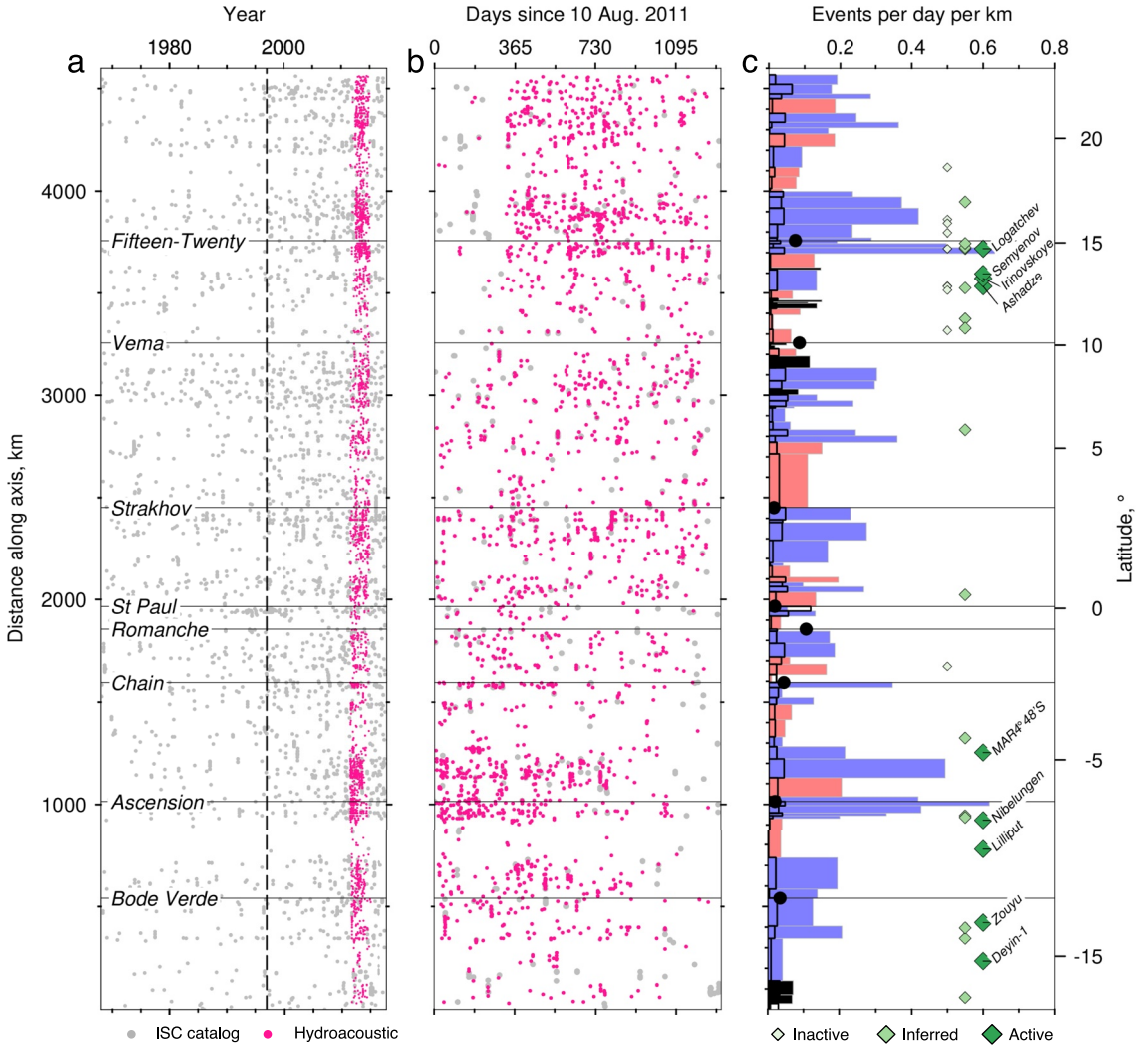

Figure 10. Seismicity and spreading style along equatorial MAR. (a) Time series of events from ISC catalog (gray dots) and hydroacoustic catalog (pink dots) 1967–2017; selected OTFs labeled; vertical dashed line indicates rapid expansion of global seismic network (GSN) station coverage that occurred in the early 1990s. (b) Time series during EA hydrophone experiment, 2011–2015. (c) Hydroacoustic seismicity. Colored bars are rate along MAR ridge segments, shaded spreading style (blue is asymmetric; red is symmetric; black is unassigned); black bars are seismicity rate from ISC catalog, 1997–2015; black dots are seismicity rate for selected OTFs; green diamonds show location of hydrothermal vents, names noted for those confirmed active (Beaulieu & Szafrański, 2020).

hydroacoustic events must correspond either to areas where spreading is accommodated by earthquakes with magnitude below the detection limit of the hydrophone array, by magmatism, or are seismically quiescent on the time scale of observation, with presumably accumulating stress. Several relatively quiet segments can be observed between the Bogdanov (7°N) and St Paul (0.75°N) transforms, near 6°30'N, 3°30'N, 2°20'N, and 2°N (Figure 7). There is relatively more hydroacoustic activity in the intervening segments, consistent with previous suggestions that variations in the mechanism by which plate spreading is accommodated varies on the second-order segment scale (e.g., Olive & Escartin, 2016). In the southern part of the study area, notable gaps in seismicity can be seen at 3°30′S (Figure 8), and centered on 9°S (south of the Ascension transform fault), where a 100 km-long segment is almost entirely aseismic (Figure 9). Interpretations in these southernmost areas are, however, preliminary, since the T-phase origins are located outside of the recording network and thus have greater location uncertainty, as shown by the poor agreement between origins and the altimetry-based position of the spreading ridge.

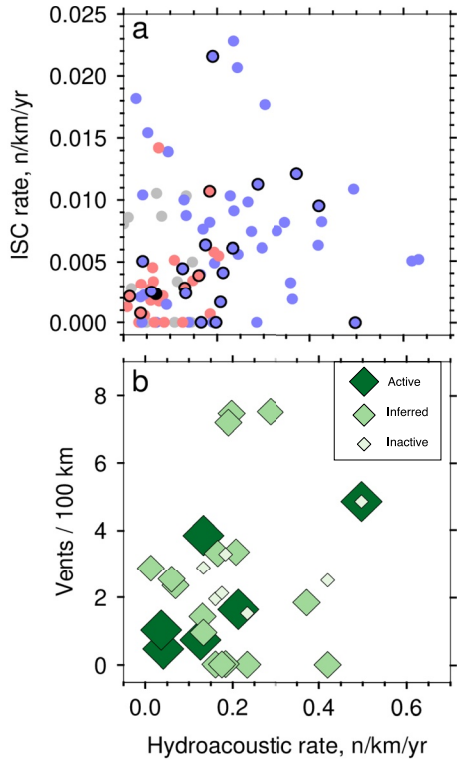

Figure 11. (a) Seismicity rate along segments of MAR (normalized by segment length and time), from ISC and hydroacoustic catalogs; blue/red dots indicate asymmetric/symmetric spreading, respectively; black outlines are segments containing hydrothermal vents (inactive, inferred or active) (Beaulieu & Szafrański, 2020). (b) Hydroacoustic seismicity rate versus hydrothermal vents per 100 km of ridge axis; green shading indicates vent type (see key).

3.2. Seismicity, Spreading Style, and Hydrothermal Venting

In order to compare observed hydroacoustic event rates with spreading style, we first identified 169 segments along the MAR using a compilation of multibeam bathymetric data (Ryan et al., 2009), extending from Oceanographer transform near 35°N, to the Gough transform near 40°'S (see Table S1 and Data Set S1). Following previous ridge axis interpretations (e.g., Gale et al., 2013; Smith & Cann, 1992; Smith et al., 2003), the spreading center was picked at the central axial high where present, and within local bathymetric deeps where not. Boundaries between segments were defined by transform faults, non-transform offsets, or distinct changes in ridge valley flank morphology when a non-transform offset was not obviously present, and hence correspond approximately to second-order segments (e.g., Macdonald et al., 1991).

The spreading style for each segment was qualitatively assigned as symmetric or asymmetric (i.e., abyssal hill bearing or detachment bearing, respectively), using shipboard multibeam bathymetric data, or inferred bathymetry from satellite altimetry if multibeam data were not available (Ryan et al., 2009), following the approach of Escartin et al. (2008). Teleseismic and hydroacoustic events located <50 km perpendicular from the ridge are expected to be associated with the spreading axis (see orange lines in Figure 5b), and the number of events meeting this criteria was normalized per day and per kilometer of spreading axis, and compared to the spreading style (Figure 10). This simple approach is likely to slightly over-estimate ridge-generated seismicity near segment ends and over-estimate the rate of transform seismicity since some events were included in both domains. Hence, seismicity rates near spreading segment ends are interpreted with caution.

Overall, there is a good visual correspondence between spreading style and seismicity rate, where asymmetric spreading segments often have higher seismicity rates than symmetric spreading segments (Figure 11a). This relationship is more obvious in the hydroacoustic catalog than in the ISC catalog, presumably due to a lower magnitude of completeness. A two-sample Student's t-test was conducted to compare the normalized hydroacoustic event rate (i.e., events per year per km of ridge axis) between symmetric and asymmetric ridge segments. There was a significant difference in the hydroacoustic event rate for asymmetric (mean = 0.224, $\sigma = 0.147$) and symmetric (mean = 0.094, $\sigma = 0.059$) segments; $t(74) = -5.55$, $p = 0.05$. There was also a significant difference in the ISC event rate for asymmetric (mean = 0.031, $\sigma = 0.019$) and symmetric (mean = 0.017, $\sigma = 0.012$) segments; $t(66) = -3.70$, $p = 0.05$. The tests show that the observed differences in seismicity between asymmetric and symmetric segments are statistically significant from each other at the 95% significance level, for both catalogs.

Segment-scale patterns in seismicity and spreading style are thought to be associated with changes in hydrothermal activity (Escartin et al., 2008), with asymmetric accretion caused by oceanic core complexes that can host both black-smoker and alkaline, Lost City-type hydrothermal systems (e.g., Charlou et al., 2002; Kelley et al., 2001; Petersen et al., 2009). We compared hydrothermal vent locations from the compilation of Beaulieu and Szafrański (2020) with accretion style and seismicity (Figure 10), and find that 8 of the 10 active confirmed vents in the equatorial MAR are located on asymmetric spreading segments, and 25 of 34 (74%) of all vents combined (including those classified as inactive, inferred, and confirmed) are on asymmetric segments. We find that the average combined vent occurrence rate for asymmetric segments is 0.97 per 100 km, nearly double the rate of 0.48 per 100 km for symmetric segments. Only considering segments with vents, there is a weakly positive relationship between hydroacoustic rate and vent occurrence, as shown in Figure 11b. This weak relationship could be explained by the large number of undiscovered vent systems in this region, meaning that the vent occurrence rate is greatly underestimated in most segments.

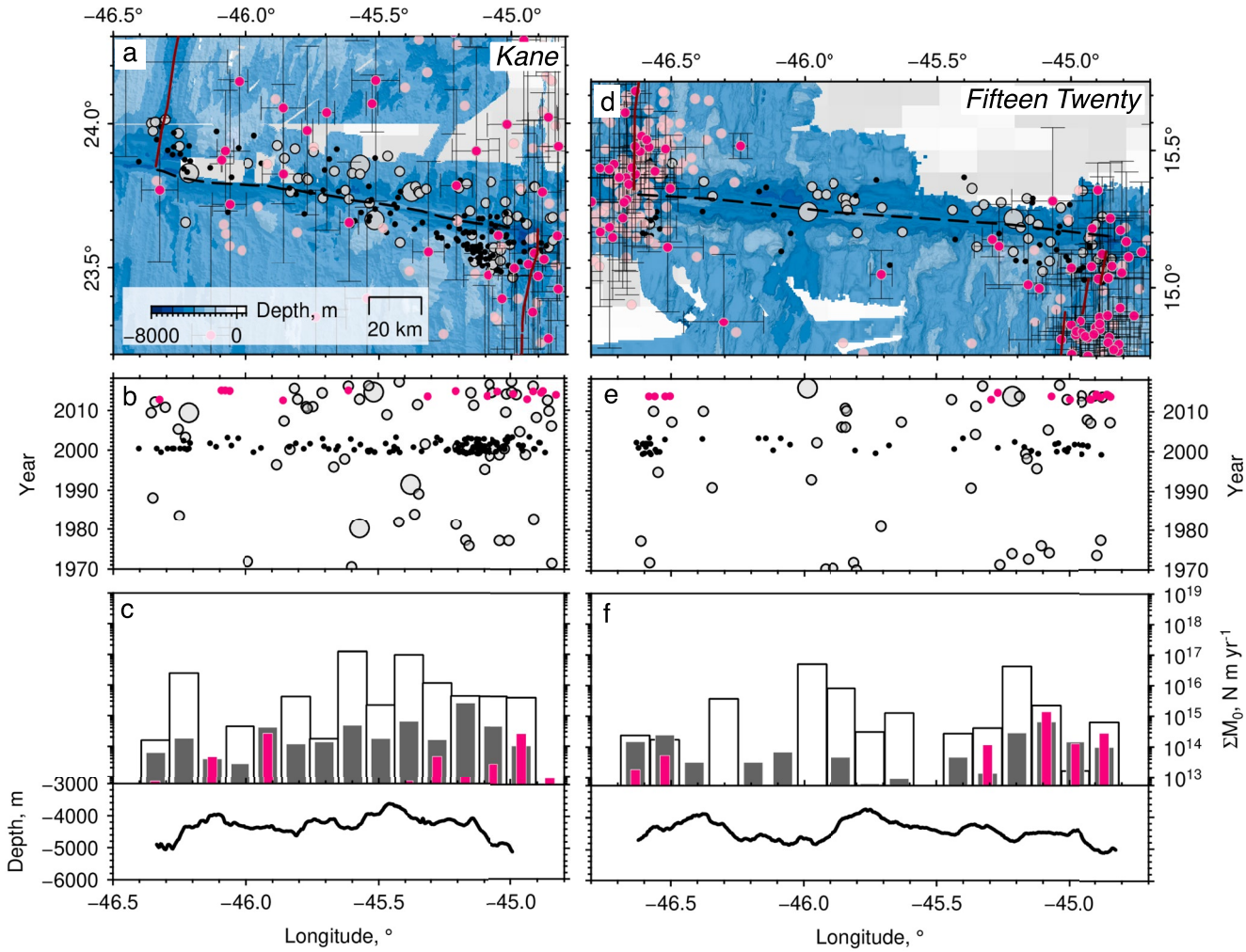

Figure 12. Seismicity on Kane and fifteen twenty ridge OTFs. (a) Kane OTF. Black/pink dots are T-phase origins from Smith et al. (2003) and this study, respectively; gray circles are ISC catalog, scaled by magnitude; dark red line is ridge axis; dashed black line is OTF trace. Note that differences in spatial coverage and hydrophone locations mean that direct comparison between NMAR and EA hydroacoustic catalogs is unreliable here (see Figure 1). (b) Time series versus longitude for T-phase origins and ISC hypocenters located within 20 km of OTF; gray lines mark edge of OTF. (c) Black line is bathymetric profile along OTF; open/gray/pink bars are ΣM_0 per year in 12 km wide bins from ISC catalog, NMAR 1999–2003 (Smith et al., 2003), and EA 2011–2015 T-phase catalogs, respectively. (d)–(f) fifteen twenty OTF.

3.3. Seismicity Along Transform Faults

Variable seismogenesis is commonly observed in both local and global studies of OTFs, probably due to along-strike variations in in fault zone properties, that cause variable coupling (e.g., Boettcher & Jordan, 2004; McGuire et al., 2012; Shi et al., 2021). Here, we use the relatively low detection threshold of the hydroacoustic catalog to explore the creeping sections of seven OTFs in the equatorial MAR (Kane, Fifteen-20, Vema, St Paul, Romanche, Chain and Ascension; Figures 12–16). Each of the OTFs examined show spatially varying seismicity, with clusters of earthquakes separated by patches of apparent creep. The bathymetric low associated with each transform was used to identify teleseismic and hydroacoustic events located <20 km perpendicular from the fault, assuming no systematic biases in our location method (see gray polygon in Figure 5b). This is a reasonable assumption since the hydrophone network was located either side of the ridge axis, without a directional bias to one side or the other. In common with the approach to assigning events to spreading segments, this method may over-estimate seismicity near transform fault tips, since some events associated with spreading center inside corner highs are likely to be included.

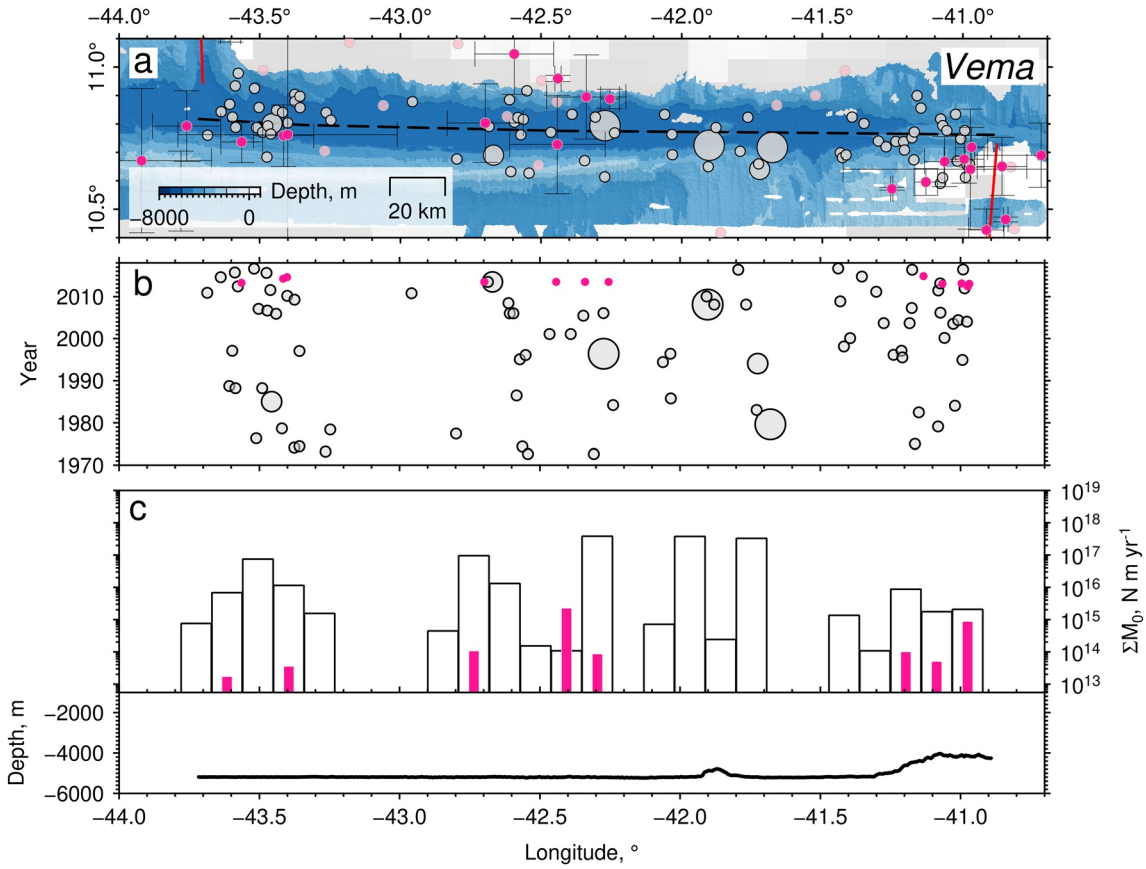

Figure 13. Seismicity on Vema OTF. (a) Pink dots are T-phase origins (this study); gray circles are ISC catalog, scaled by magnitude; dark red line is ridge axis; dashed black line is OTF trace. (b) Time series versus longitude for T-phase origins and ISC hypocenters located within 20 km of OTF; gray lines mark edge of OTF. (c) Black line is bathymetric profile along OTF; open/pink bars are ΣM_0 per year in 12 km wide bins from ISC catalog and EA 2011–2015 T-phase catalogs, respectively.

Seismicity on the fifteen twenty OTF is restricted to the ends of the fault, and is nearly absent altogether in the center, except for a small patch of seismicity between 45.8 and 46.0°W (Figure 12). Times series constructed using a combination of events from the ISC catalog and events in the NMAR and EA hydroacoustic catalogs show that this aseismic pattern has likely persisted for several decades. Two clear zones of aseismic behavior can also be seen at the Vema OTF near 43°W and 41.5°W, separated by a ∼100 km-long central fault section, which has hosted two $M_w > 5$ events since 1995 (Figure 13).

Relatively high rates of seismicity can be seen in the hydroacoustic catalog centered at 29.5°W on the St Paul OTF, coinciding with the Atobá Ridge, which is subaerially exposed at the St Peter and St Paul Islets (Figure 14). These events are mostly concentrated to the west of the islets themselves and are likely due to transpressive shear stresses associated with southward migration of the MAR being accommodated by bends and offsets in the St Paul OTF (Maia et al., 2016).

Considerable variations in seismicity can be observed at the 880 km-long Romanche OTF, which is known to have hosted $M_w > 7$ events in 1982, 1994, and 2016 (Figure 15; Abercrombie & Ekstrom, 2003; Hicks et al., 2020; McGuire et al., 1996). A ∼100 km-long aseismic patch is centered at 22.5°W and is clearly evident in both ISC and hydroacoustic catalogs. This patch coincides with the point of shallowest bathymetry on the Romanche OTF, which rises ∼2,000 m above the deeper floor of the OTF to the east and west. We compared the trend of the bathymetric trace of the north and south transform fault scarps to the trace of small circles calculated using the South America-Nubia stage pole for 0–781 ka located at 38.74°W 60.35°N (Demets & Merkouriev, 2019). In the eastern portion of the Romanche OTF, the fault scarp azimuthal trend is broadly parallel with the rotation associated with the small-circle trace predicted by the stage pole (Figure 15); however, there is an abrupt northward change in azimuth of the southern fault scarp near 22.5°W, resulting in a deviation from the small-circle trend.

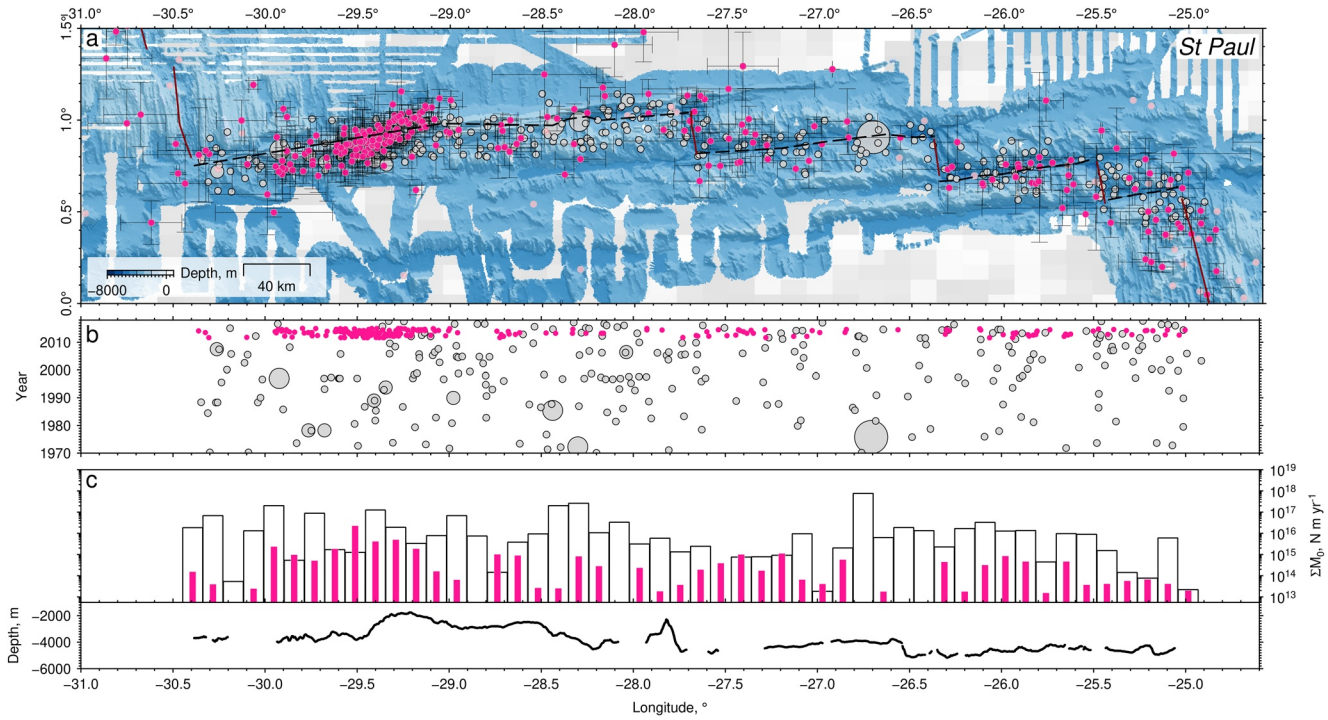

Figure 14. Seismicity on St Paul OTF. (a) Pink dots are T-phase origins (this study); gray circles are ISC catalog, scaled by magnitude; dark red line is ridge axis; dashed black line is OTF trace. (b) Time series versus longitude for T-phase origins and ISC hypocenters located within 20 km of OTF; gray lines mark edge of OTF. (c) Black line is bathymetric profile along OTF; open/pink bars are ΣM_0 per year in 12 km wide bins from ISC catalog and EA 2011–2015 T-phase catalogs, respectively.

This change in fault azimuth coincides with the bathymetric high, and also the patch of reduced hydroacoustic seismicity. We speculate that a recent, regional clockwise rotation may have caused the transform trend to deviate northward, resulting in increased transpressive stress and vertical uplift of the the western end of the Romanche OTF. Increased compressional stress perpendicular to this section of the Romanche OTF might inhibit slip, and could result in this segment of the fault being locked. Alternatively, uplift could coincide with upward-bending of the lithosphere, which would tend to open cracks near the surface and favor fluid delivery to the fault damage zone and perhaps lead to the increased presence of low-friction minerals such as talc and serpentine, leading to aseismic creep. In the southern portion of the equatorial Atlantic, seismicity on the Chain and Ascension OTFs is frequent, with notable gaps in the hydroacoustic and teleseismic catalogs (Figure 16). Bathymetric data coverage is poor here, in particular at the Chain OTF, hampering further detailed interpretation.

3.4. Hydroacoustic Detection of Foreshocks

Large earthquakes on OTFs are thought to be commonly preceded by foreshocks, associated with fluid-related processes that alter the fault zone properties prior to a main rupture (e.g., Dziak et al., 2003; McGuire et al., 2005, 2012). Numerical models show that in near ridge-transform intersections where the fault is relatively hot, considerable variations in fluid compressibility may arise, leading to a metastable plastic condition in the fault zone that can generate foreshock swarms (Géli et al., 2014). We use the hydroacoustic catalog to examine anomalous foreshock sequences associated with earthquakes on the equatorial Atlantic OTFs.

Precursor activity was analyzed for events $M_w > 5.0$ in the GCMT catalog (Ekström et al., 2012) coincident with the EA experiment (August 2011–January 2015) and located between 15°S and 20°N ($n = 111$). The GCMT catalog was chosen for this purpose in order to consider differences in main shock faulting mechanism in our analysis, and events were categorized as strike-slip ($n = 57$) and non strike-slip ($n = 54$) based on the reported rake (see Figure 17). We then searched for precursors in the hydroacoustic catalog with onset times within ±80 hr of each GCMT mainshock, and calculated the distance between candidate mainshock-aftershock/precursor pairs.

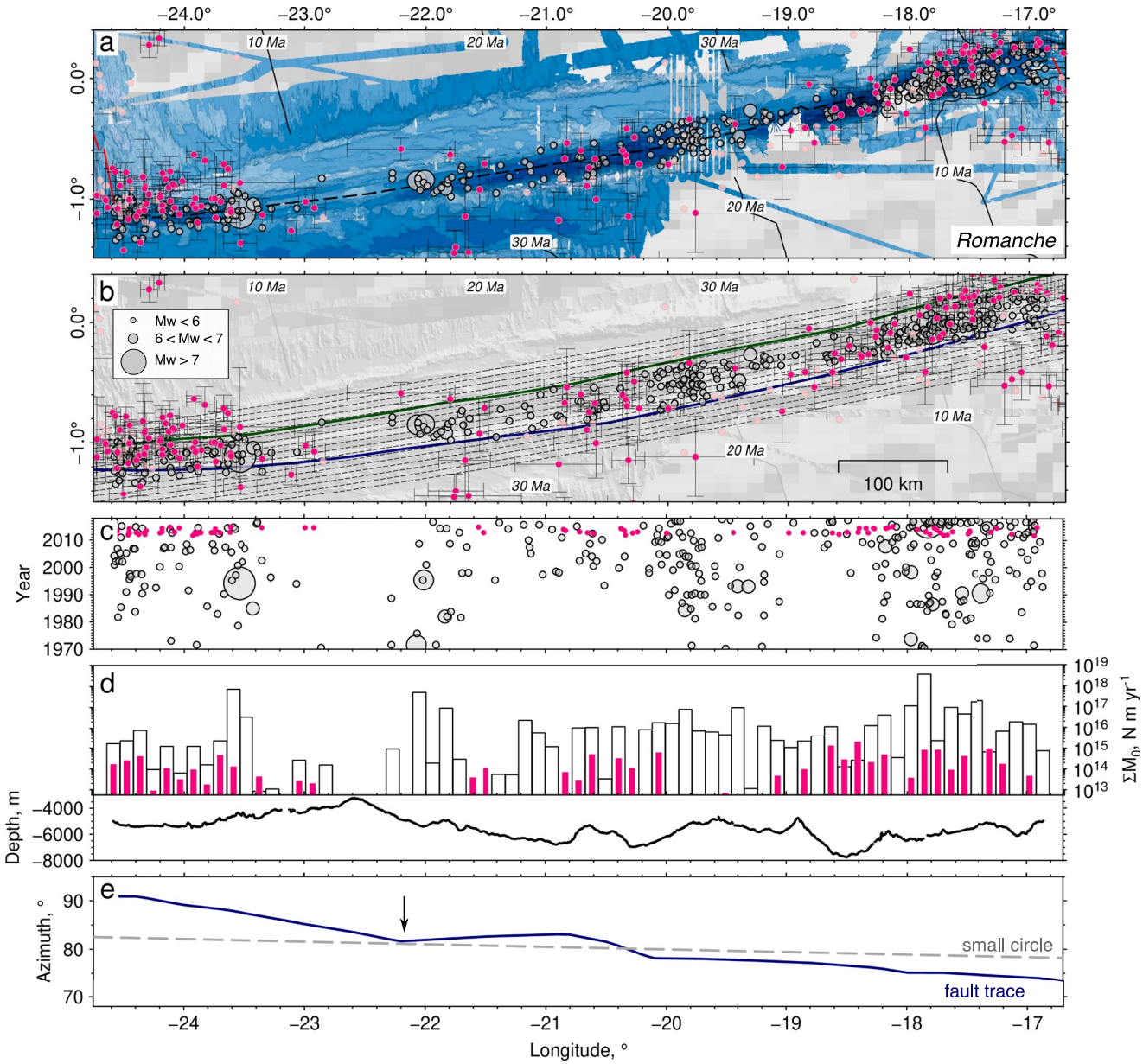

Figure 15. Seismicity on Romanche OTF. (a) Pink dots are T-phase origins (this study); gray circles are ISC catalog, scaled by magnitude; dark red line is ridge axis; dashed black line is OTF trace; black labeled contours are isochrons (Müller et al., 2008). (b) Transform valley interpretation. Blue/green lines are interpreted south/north transform valley edges, respectively; dotted lines are small circles calculated for stage pole at 38.74°W 60.35°N (Demets & Merkouriev, 2019). (c) Time series versus longitude for T-phase origins and ISC hypocenters located within 20 km of OTF. (d) Black line is bathymetric profile along OTF; open/pink bars are ΣM_0 per year in 12 km-wide bins from ISC catalog and EA 2011–2015 T-phase catalogs, respectively. (e) Azimuth of small circles (gray) and southern transform valley edge (blue). Note bend onset near 22.1°W (arrow), where azimuthal trends diverge, coinciding with change in bathymetry and seismicity.

We find that strike-slip events (red dots in Figure 17) have relatively few precursors or aftershocks, whereas non strike-slips events, which are nearly all associated with normal faulting (blue dots in Figure 17), have frequent precursors and aftershocks.

The long time window and wide search area in Figure 17a shows low levels of background seismicity up to ~24 hr before each main shock and a rapidly decaying rate of aftershocks. A closer examination of the foreshocks within 20 km and 2 hr of the main shock reveals a modest increase in the rate of seismicity close to the main shock (Figure 17), similar to the accelerating rate of seismicity observed for the Discovery and Gofar OTFs in the eastern Pacific ocean (McGuire et al., 2005, 2012). Unlike these earlier studies, however, we find that

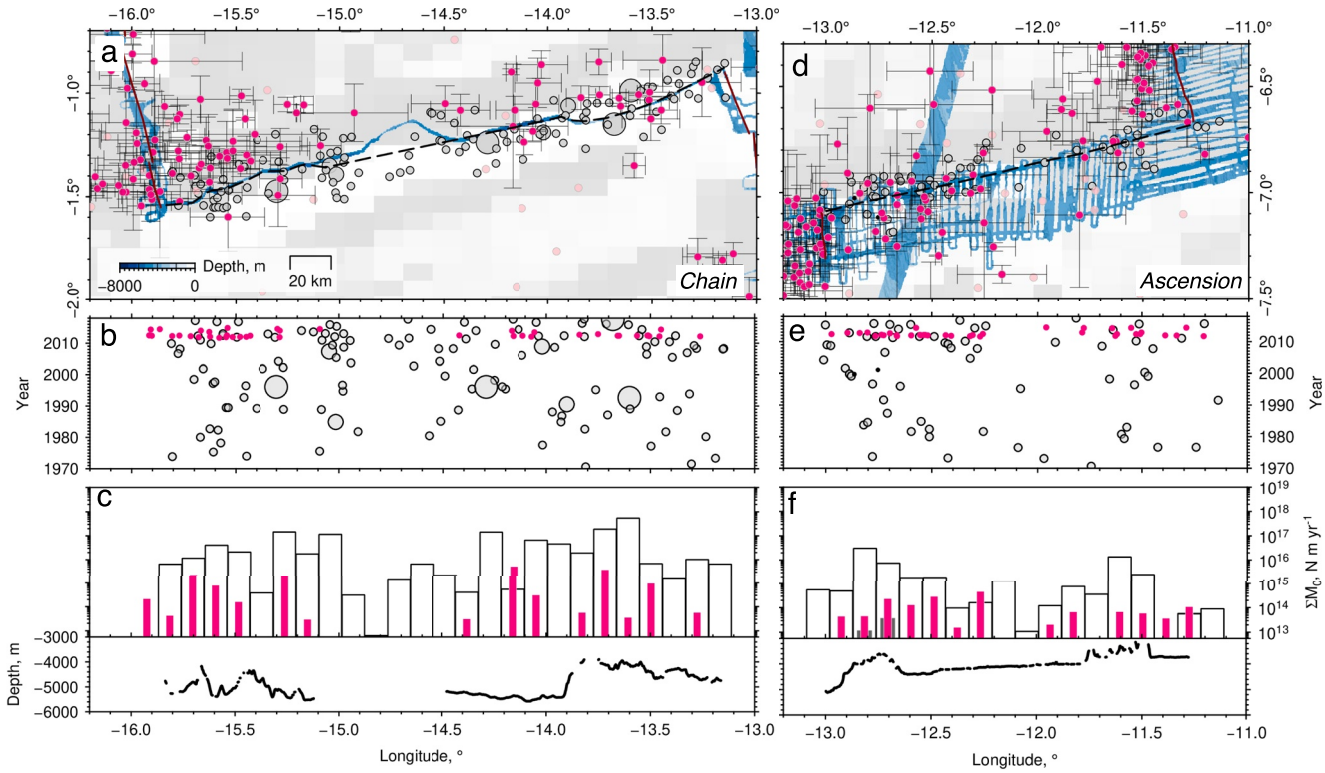

Figure 16. Seismicity on chain and ascension OTFs. (a) Chain OTF. Pink dots are T-phase origins (this study); gray circles are ISC catalog, scaled by magnitude; dark red line is ridge axis; dashed black line is OTF trace. (b) Time series versus longitude for T-phase origins and ISC hypocenters located within 20 km of OTF; gray lines mark edge of OTF. (c) Black line is bathymetric profile along OTF; open/pink bars areΣM_0 per year in 12 km wide bins from ISC catalog and EA 2011–2015 T-phase catalogs, respectively. (d)–(f) Ascension OTF.

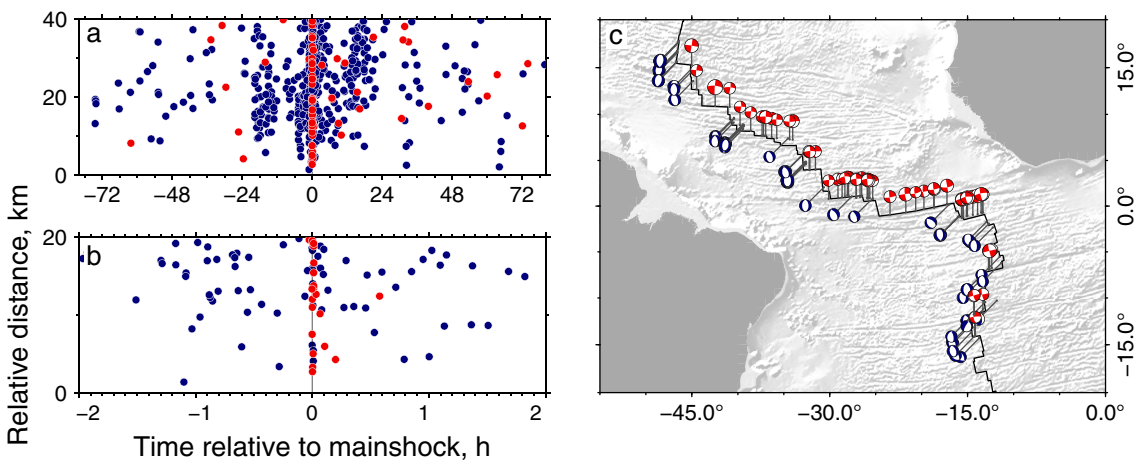

Figure 17. Space-time distribution of seismicity around 111 mainshocks (M_w > 5.0) from GCMT catalog between August 2011 and January 2015 (Ekström et al., 2012). (a) Stack of all events from groomed hydroacoustic catalog (this study) located within ±40 km along strike and within ±80 hr of mainshocks; negative time indicates precursors, positive time indicates aftershocks; red/blue dots are hydroacoustic events associated with strike-slip and non-strike slip main shocks, respectively. (b) Zoomed-in view of seismicity, showing foreshock activity within ±2 hr and 20 km of mainshocks, colors as in panel (a). (c) Map showing location and centroid moment tensors of main shocks from GCMT catalog used in (a); red/blue shading shows strike-slip (n = 54) and non-strike slip (n = 57) events, respectively.

normal faulting events on the ridge axis are more likely to exhibit precursor behavior than transform-fault hosted strike-slip events. Although these precursor detections are based upon a relatively small number of main shocks and are hence preliminary, these observations suggest that further investigation into precursor events associated with mid-ocean ridge normal faulting is warranted.

4. Conclusions

Waveforms recorded by an array of 10 autonomous hydrophones covering an area from 20°N to 10°S in the equatorial Atlantic Ocean were used to generate a catalog of 6,843 hydroacoustic events between August 2011 and January 2015. The hydroacoustic event catalog has a magnitude of completeness of 3.3, roughly an order of magnitude lower than the ISC teleseismic catalog (4.4). We find that hydroacoustic event rate correlates with crustal accretion style, and consistent with previous studies (e.g., Escartin et al., 2008), asymmetric spreading segments have a statistically significant higher event rate at 95% confidence interval than symmetric segments. Asymmetric spreading segments are also more likely to host hydrothermal vents than symmetric segments, with twice as many vents per 100 km of ridge axis, implying that many vents likely remain to be identified along the MAR. Patterns of events in the hydroacoustic catalog support the idea that aseismic patches are ubiquitous on OTFs in the equatorial Atlantic ocean, including the aseismic patch on Romanche OTF, which could be explained by changing fault scarp trend with respect to the pole of rotation. Normal faulting events ($M_w > 5.0$) are often associated with modest increases in seismicity rates beginning ~24 hr prior to the main shock, suggesting that precursor seismicity could be common on mid-ocean ridge spreading segments.

Data Availability Statement

The T-phase catalog including station coordinates used in this study are archived at the Marine Geoscience Data System via https://www.marine-geo.org/tools/search/entry.php?id=EA_Hydroacoustics and via https://doi.org/10.26022/IEDA/330497 (Parnell-Turner et al., 2022). Teleseismic earthquake locations used in this work were obtained from the International Seismological Centre Bulletin online, via https://doi.org/10.31905/D808B830. Centroid moment tensor solutions were obtained from the GCMT catalog (Ekström et al., 2012). The digitized second-order ridge segments for the equatorial Atlantic ocean are provided as a zipped file in the Supporting Information Data Set S1. Figures were created using the Generic Mapping Tools, version 6 (Wessel et al., 2013).

Acknowledgments
Waveform data were provided through the virtual Data Exploitation Centre (vDEC), within the framework of an agreement between the Comprehensive Nuclear-Test-Ban Treaty Organization (CTBTO) and the University of California, San Diego. This research was supported by National Science Foundation Grants EAR-1062238, EAR-1062165, and OCE-1839727. We thank J. Braunmiller and an anonymous reviewer, whose detailed comments helped us to improve our work. This paper is NOAA Pacific Marine Environmental Laboratory contribution 5323.

References

Abercrombie, R. E., & Ekstrom, G. (2003). A reassessment of the rupture characteristics of oceanic transform earthquakes. *Journal of Geophysical Research*, *108*(B5). https://doi.org/10.1029/2001JB000814

Aderhold, K., & Abercrombie, R. E. (2016). The 2015 Mw 7.1 earthquake on the Charlie-Gibbs transform fault: Repeating earthquakes and multimodal slip on a slow oceanic transform. *Geophysical Research Letters*, *43*(12), 6119–6128. https://doi.org/10.1002/2016GL068802

Aki, K. (1965). Maximum likelihood estimate of b in the formula log N = a-bM and its confidence limits. *Bulletin of the Earthquake Research Institute Tokyo University*, *43*, 237–239.

Beaulieu, S. E., & Szafrański, K. M. (2020). InterRidge global Database of active Submarine hydrothermal vent Fields version 3.4. *Pangea*. https://doi.org/10.1594/PANGAEA.917894

Blackman, D. K., & Forsyth, D. W. (1991). Isostatic compensation of tectonic features of the mid-Atlantic Ridge - 25-27°30's. *Journal of Geophysical Research*, *96*(B7), 11741–11758. https://doi.org/10.1029/91jb00602

Boettcher, M. S., & Jordan, T. H. (2004). Earthquake scaling relations for mid-ocean ridge transform faults. *Journal of Geophysical Research B: Solid Earth*, *109*(12), 1–21. https://doi.org/10.1029/2004JB003110

Bohnenstiehl, D. R., & Kleinrock, M. (2000). Evidence for spreading-rate dependence in the displacement-length ratios of abyssal hill faults at mid-ocean ridges. *Geology*, *28*(5), 395–398. https://doi.org/10.1130/0091-7613(2000)028<0395:efsrdi>2.3.co;2

Bohnenstiehl, D. R., Tolstoy, M., Dziak, R. P., Fox, C. G., & Smith, D. K. (2002). Aftershock sequences in the mid-ocean ridge environment: An analysis using hydroacoustic data. *Tectonophysics*, *354*(1–2), 49–70. https://doi.org/10.1016/S0040-1951(02)00289-5

Bohnenstiehl, D. R., Tolstoy, M., Smith, D. K., Fox, C. G., & Dziak, R. P. (2003). Time-clustering behavior of spreading-center seismicity between 15 and 35°N on the Mid-Atlantic Ridge: Observations from hydroacoustic monitoring. *Physics of the Earth and Planetary Interiors*, *138*(2), 147–161. https://doi.org/10.1016/S0031-9201(03)00113-4

Bonatti, E. (1996). Anomalous opening of the Equatorial Atlantic due to an equatorial mantle thermal minimum. *Earth and Planetary Science Letters*, *43*(96), 147–160. https://doi.org/10.1016/0012-821x(96)00125-2

Bonatti, E., Ligi, M., Gaspcrini, L., Payve, A., Raznitsin, Y., Chen, Y. J., et al. (1994). Transform migration and vertical tectonics at the Romanche fracture zone, equatorial Atlantic. *Journal of Geophysical Research*, *99802*(21), 779–821. https://doi.org/10.1029/94JB01178

Braunmiller, J., & Nábělek, J. (2008). Segmentation of the Blanco Transform Fault Zone from earthquake analysis: Complex tectonics of an oceanic transform fault. *Journal of Geophysical Research*, *113*(7), 1–23. https://doi.org/10.1029/2007JB005213

Brune, J. (1968). Seismic moment, seismicity, and rate of slip along major fault zones. *Journal of Geophysical Research*, *73*(2), 777–784. https://doi.org/10.1029/jb073i002p00777

Cann, J. R., Blackman, D. K., Smith, D. K., McAllister, E., Janssen, B., Mello, S., et al. (1997). Corrugated slip surfaces formed at ridge-transform intersections on the Mid-Atlantic Ridge. *Nature*, *385*, 329–332. https://doi.org/10.1038/385329a0

Cannat, M., Mevel, C., Maia, M., Deplus, C., Durand, C., Gente, P., et al. (1995). Thin crust, ultramafic exposures, and rugged faulting patterns at the Mid-Atlantic Ridge (22°–24°N). *Geology*, *23*, 49–52. https://doi.org/10.1130/0091-7613(1995)023<0049:tcuear>2.3.co;2

Charlou, J. L., Donval, J. J., Fouquet, Y., Jean-Baptiste, P., & Holm, N. (2002). Geochemistry of H2 and CH4 vent fluids issuing from ultramafic rocks at Rainbow hydrothermal field. *Chemical Geology*, *191*(4), 345–359. https://doi.org/10.1016/S0009-2541(02)00134-1

Das, R., Wason, H. R., & Sharma, M. L. (2011). Global regression relations for conversion of surface wave and body wave magnitudes to moment magnitude. *Natural Hazards*, *59*(2), 801–810. https://doi.org/10.1007/s11069-011-9796-6

de Groot-Hedlin, C. D., & Orcutt, J. A. (2001). Excitation of T -phases by seafloor scattering. *Journal of the Acoustical Society of America*, *109*(5), 1944–1954. https://doi.org/10.1121/1.1361057

Demets, C., & Merkouriev, S. (2019). High-resolution reconstructions of south America plate motion relative to Africa, Antarctica and North America: 34 Ma to present. *Geophysical Journal International*, *217*(3), 1821–1853. https://doi.org/10.1093/gji/ggz087

Dick, H. J. B., Lin, J., & Schouten, H. (2003). An ultraslow-spreading class of ocean ridge. *Nature*, *426*, 405–412. https://doi.org/10.1038/nature02128

Dziak, R. P. (2001). Empirical relationship of T-wave energy and fault parameters of Northeast Pacific Ocean earthquakes. *Geophysical Research Letters*, *28*(13), 2537–2540. https://doi.org/10.1029/2001GL012939

Dziak, R. P., Bohnenstiehl, D. R., Matsumoto, H., Fox, C. G., Smith, D. K., Tolstoy, M., et al. (2004). P- and T-wave detection thresholds, Pn velocity estimate, and detection of lower mantle and core P-waves on ocean sound-channel hydrophones at the Mid-Atlantic Ridge. *Bulletin of the Seismological Society of America*, *94*(2), 665–677. https://doi.org/10.1785/0120030156

Dziak, R. P., Chadwick, W. W., Fox, C. G., & Embley, R. W. (2003). Hydrothermal temperature changes at the southern juan de Fuca ridge associated with a Mw 6.2 Blanco transform earthquake. *Geology*, *31*(2), 119–122. https://doi.org/10.1130/0091-7613(2003)031<0119:htcats>2.0.co;2

Dziak, R. P., Fox, C. G., Matsumoto, H., & Schreiner, A. E. (1997). The April 1992 Cape Mendocino earthquake sequence: Seismo-acoustic analysis utilizing fixed hydrophone arrays. *Marine Geophysical Research*, *19*(2), 137–162. https://doi.org/10.1023/A:1004256910362

Ekström, G., Nettles, M., & Dziewoński, A. M. (2012). The global CMT project 2004–2010: Centroid-moment tensors for 13,017 earthquakes. *Physics of the Earth and Planetary Interiors*, 200–201. 1–9. https://doi.org/10.1016/j.pepi.2012.04.002

Escartin, J., Smith, D. K., Cann, J. R., Schouten, H., Langmuir, C. H., & Escrig, S. (2008). Central role of detachment faults in accretion of slow-spreading oceanic lithosphere. *Nature*, *455*(7214), 790–794. https://doi.org/10.1038/nature07333

Escartin, J., Smith, D. K., & Cannat, M. (2003). Parallel bands of seismicity at the mid-Atlantic Ridge, 12–14°N. *Geophysical Research Letters*, *30*(12), 1620. https://doi.org/10.1029/2003GL017226

Fox, C. G., Matsumoto, H., & Lau, T.-K. A. T. K. A. (2001). Monitoring Pacific Ocean seismicity from an autonomous hydrophone array. *Journal of Geophysical Research*, *106*(10), 41834206. https://doi.org/10.1029/2000JB900404

Fox, C. G., Radford, W. E., Dziak, R. P., Lau, T. K., Matsumoto, H., & Schreiner, A. E. (1995). Acoustic detection of a seafloor spreading episode on the Juan de Fuca Ridge using military hydrophone arrays. *Geophysical Research Letters*, *22*(2), 131–134. https://doi.org/10.1029/94GL02059

Frohlich, C. (2007). Practical suggestions for assessing rates of seismic-moment release. *Bulletin of the Seismological Society of America*, *97*(4), 1158–1166. https://doi.org/10.1785/0120060193

Frohlich, C., & Davis, S. D. (1993). Teleseismic b values; or, much ado about 1.0. *Journal of Geophysical Research*, *98*(B1), 631–644. https://doi.org/10.1029/92JB01891

Gale, A., Dalton, C. A., Langmuir, C. H., & Su, Y. (2013). The mean composition of ocean ridge basalts. *Geochemistry, Geophysics, Geosystems*, *14*(2009). https://doi.org/10.1029/2012GC004334

Géli, L., Piau, J. M., Dziak, R., Maury, V., Fitzenz, D., Coutellier, Q., & Henry, P. (2014). Seismic precursors linked to super-critical fluids at oceanic transform faults. *Nature Geoscience*, *7*(10), 757–761. https://doi.org/10.1038/NGEO2244

Gong, J., Fan, W., & Parnell-Turner, R. E. (2022). Microseismicity indicates atypical small-scale plate rotation at the Quebrada transform fault system, East Pacific Rise. *Geophysical Research Letters*. https://doi.org/10.1029/2021gl097000

Gregg, P. M., Lin, J., Behn, M. D., & Montési, L. G. J. (2007). Spreading rate dependence of gravity anomalies along oceanic transform faults. *Nature*, *448*(7150), 183–187. https://doi.org/10.1038/nature05962

Hicks, S. P., Okuwaki, R., Steinberg, A., Rychert, C. A., Harmon, N., Abercrombie, R. E., et al. (2020). Back-propagating supershear rupture in the 2016 M w 7.1 Romanche transform fault earthquake. *Nature Geoscience*, *13*(9), 647–653. https://doi.org/10.1038/s41561-020-0619-9

International Seismological Centre. (2022). On-line Bulletin. https://doi.org/10.31905/D808B830

Johnson, R. H. (1966). Routine location of T-phase sources in the Pacific. *Bulletin of the Seismological Society of America*, *56*(1), 109–118. https://doi.org/10.1785/bssa0560010109

Jones, E. J. (1987). Fracture zones in the equatorial Atlantic and the breakup of Western Pangea. *Geology*, *15*(6), 533–536. https://doi.org/10.1130/0091-7613(1987)15h533:FZITEAi2.0.CO;2

Kanamori, H. (1983). Magnitude scale and quantification of earthquakes. *Tectonophysics*, *93*, 185–199. https://doi.org/10.1016/0040-1951(83)90273-1

Kelley, D., Karson, J. A., Blackman, D. K., Früh-Green, G., Butterfield, D. A., Lilley, M. D., et al. (2001). An off-axis hydrothermal vent near the Mid-Atlantic Ridge at 30° N. *Nature*, *412*, 145–149. https://doi.org/10.1038/35084000

Klitgord, K., & Schouten, H. (1986). Plate kinematics of the central Atlantic. In P. R. Vogt, & B. E. Tucholke (Eds.), *The Geology of North America, The Western North Atlantic Region*. Geological Society of America.

Kuo, B.-Y., & Forsyth, D. W. (1988). Gravity anomalies of the ridge-transform system in the south atlantic between 31 and 34.5 S: Upwelling centers and variations in crustal thickness. *Marine Geophysical Researches*, *10*, 205–232. https://doi.org/10.1007/bf00310065

Le Pichon, X., & Fox, P. J. (1971). Marginal offsets, fracture zones, and the early opening of the North Atlantic. *Journal of Geophysical Research*, *76*(26), 6294–6308. https://doi.org/10.1029/jb076i026p06294

Macdonald, K. C., Scheirer, D. S., & Carbotte, S. M. (1991). Mid-ocean ridges: Discontinuities, segments and giant cracks. *Science*, *253*(5023), 986. https://doi.org/10.1126/science.253.5023.986

Maia, M., Sichel, S., Briais, A., Brunelli, D., Ligi, M., Ferreira, N., et al. (2016). Extreme mantle uplift and exhumation along a transpressive transform fault. *Nature Geoscience*, *9*(8), 619–623. https://doi.org/10.1038/ngeo2759

McGuire, J. J., Boettcher, M. S., & Jordan, T. H. (2005). Foreshock sequences and short-term earthquake predictability on East Pacific Rise transform faults. *Nature*, *434*, 457–462. https://doi.org/10.1038/nature03377

McGuire, J. J., Collins, J. A., Gouédard, P., Roland, E., Lizarralde, D., Boettcher, M. S., et al. (2012). Variations in earthquake rupture properties along the Gofar transform fault, East Pacific Rise. *Nature Geoscience*, *5*(5), 336–341. https://doi.org/10.1038/ngeo1454

McGuire, J. J., Ihmle, P. F., & Jordan, T. H. (1996). Time-domain observations of a slow precursor to the 1994 Romanche transform earthquake. *Science*, *274*, 82–85. https://doi.org/10.1126/science.274.5284.82

Müller, R. D., Sdrolias, M., Gaina, C., & Roest, W. R. (2008). Age, spreading rates, and spreading asymmetry of the world's ocean crust. *Geochemistry, Geophysics, Geosystems*, *9*(4), 1–19. doi: https://doi.org/10.1029/2007GC001743

Okal, E. A. (2001). T-Phase stations for the international monitoring system of the comprehensive nuclear-test ban treaty: A global perspective. *Seismological Research Letters*, *72*(2), 186–196. https://doi.org/10.1785/gssrl.72.2.186

Okal, E. A. (2008). The generation of T waves by earthquakes. *Advances in Geophysics*, *49*, 1–65. https://doi.org/10.1016/S0065-2687(07)49001-X

Oldenburg, D. W., & Brune, J. N. (1972). Ridge transform fault spreading pattern in freezing wax. *Science*, *178*(4058), 301–304. https://doi.org/10.1126/science.178.4058.301

Olive, J.-A., Behn, M. D., & Tucholke, B. E. (2010). The structure of oceanic core complexes controlled by the depth distribution of magma emplacement. *Nature Geoscience*, *3*(7), 491–495. https://doi.org/10.1038/ngeo888

Olive, J.-A., & Escartin, J. (2016). Dependence of seismic coupling on normal fault style along the Northern Mid-Atlantic Ridge. *Geochemistry, Geophysics, Geosystems*, *17*(10), 4128–4152. https://doi.org/10.1002/2016GC006460

Pan, J., & Dziewonski, A. M. (2005). Comparison of mid-oceanic earthquake epicentral differences of travel time, centroid locations, and those determined by autonomous underwater hydrophone arrays. *Journal of Geophysical Research*, *110*, 1–21. https://doi.org/10.1029/2003JB002785

Parnell-Turner, R., Dziak, R. P., & Smith, D. K. (2022). T-phase location catalog for equatorial Atlantic ocean, 2011–2015. *IEDA*. https://doi.org/10.26022/IEDA/330497

Petersen, S., Kuhn, K., Kuhn, T., Augustin, N., Hékinian, R., Franz, L., & Borowski, C. (2009). The geological setting of the ultramafic-hosted Logatchev hydrothermal field (14°45N, Mid-Atlantic Ridge) and its influence on massive sulfide formation. *Lithos*, *112*(1–2), 40–56. https://doi.org/10.1016/j.lithos.2009.02.008

Ryan, W. B. F., Carbotte, S. M., Coplan, J. O., Hara, S. O., Melkonian, A., Arko, R., et al. (2009). Global Multi-resolution topography synthesis. *Geochemistry, Geophysics, Geosystems*, *10*(3). https://doi.org/10.1029/2008GC002332

Shi, P., Wei, M. M., & Pockalny, R. (2021). The ubiquitous creeping segments on oceanic transform faults. *Geology*. https://doi.org/10.1130/G49562.1/5456015/g49562.pdf

Simão, N., Escartin, J., Goslin, J., Haxel, J., Cannat, M., & Dziak, R. P. (2010). Regional seismicity of the mid-Atlantic Ridge: Observations from autonomous hydrophone arrays. *Geophysical Journal International*, *183*(3), 1559–1578. doi: https://doi.org/10.1111/j.1365?246X.2010.04815

Slack, P., Fox, C. G., & Dziak, R. P. (1999). P wave detection thresholds, Pn velocity estimates, and T wave location uncertainty from oceanic hydrophones. *Journal of Geophysical Research*, *104*, 61–72. doi: https://doi.org/10.1029/1999jb900112

Smith, D. K., & Cann, J. R. (1992). The role of seamount volcanism in crustal construction at the Mid-Atlantic Ridge (24-30°N). *Journal of Geophysical Research*, *97*(B2), 1645–1658. doi: 10.1029/91jb02507

Smith, D. K., Cann, J. R., & Escartin, J. (2006). Widespread active detachment faulting and core complex formation near 13°N on the Mid-Atlantic. *Nature*, *442*, 440–443. https://doi.org/10.1038/nature04950

Smith, D. K., Escartin, J., Cannat, M., Tolstoy, M., Fox, C. G., Bohnenstiehl, D. R., & Bazin, S. (2003). Spatial and temporal distribution of seismicity along the northern Mid-Atlantic Ridge (15°–35°N). *Journal of Geophysical Research*, *108*(B3). https://doi.org/10.1029/2002JB001964

Smith, D. K., Escartin, J., Schouten, H., & Cann, J. R. (2008). Fault rotation and core complex formation: Significant processes in seafloor formation at slow-spreading mid-ocean ridges (Mid-Atlantic Ridge, 13°–15°N). *Geochemistry, Geophysics, Geosystems*, *9*(3). https://doi.org/10.1029/2007GC001699

Smith, D. K., Tolstoy, M., Fox, C. G., Bohnenstiehl, D. R., Matsumoto, H., & Fowler, M. (2002). Hydroacoustic monitoring of seismicity at the slow-spreading Mid-Atlantic Ridge. *Geophysical Research Letters*, *29*. https://doi.org/10.1029/2001gl013912

Sykes, L. R. (1967). Mechanism of earthquakes and nature of faulting on the mid-oceanic ridges. *Journal of Geophysical Research*, *72*(8), 2131–2153. https://doi.org/10.1029/JZ072i008p02131

Talandier, J., & Okal, E. A. (1998). On the mechanism of conversion of seismic waves to and from T waves in the vicinity of island shores. *Bulletin of the Seismological Society of America*, *88*(2), 621–632.

Teague, W. J., Carron, M. J., & Hogan, P. J. (1990). A comparison between the generalized digital environmental model and Levitus climatologies. *Journal of Geophysical Research*, *95*(C5), 7167–7183. https://doi.org/10.1029/JC095iC05p07167

Tucholke, B. E., Lin, J., & Kleinrock, M. C. (1998). Megamullions and mullion structure defining oceanic metamorphic core complexes on the Mid-Atlantic Ridge. *Journal of Geophysical Research*, *103*(B5), 9857–9866. https://doi.org/10.1029/98jb00167

Uchupi, E. (1989). The tectonic style of the atlantic mesozoic rift system. *Journal of African Earth Sciences*, *8*(2–4), 143–164. https://doi.org/10.1016/S0899-5362(89)80021-1

Wessel, P., Smith, W. H. F., Scharoo, R., Luis, J., & Wobbe, F. (2013). Generic mapping Tools: Improved version released. *Eos, Transactions American Geophysical Union*, *94*(45), 409–410. https://doi.org/10.1002/2013eo450001

Wiemer, S., & Wyss, M. (2000). Minimum magnitude of completeness in earthquake catalogs: Examples from Alaska, the Western United States, and Japan. *Bulletin of the Seismological Society of America*, *90*, 859–869. https://doi.org/10.1785/0119990114

Williams, C. M., Stephen, R. A., & Smith, D. K. (2006). Hydroacoustic events located at the intersection of the Atlantis (30N) and Kane (23 40'N) transform faults with the Mid-Atlantic Ridge. *Geochemistry, Geophysics, Geosystems*, *7*. https://doi.org/10.1029/2005GC001127

Wilson, J. T. (1965). A new class of faults and their bearing on continental drift. *Nature*, *4995*, 343–347. https://doi.org/10.1038/207343a0

Wolfson-Schwehr, M., & Boettcher, M. S. (2018). Global characteristics of oceanic transform fault structure and seismicity. In *Transform plate boundaries and fracture zones* (pp. 21–59). Elsevier Inc. https://doi.org/10.1016/B978-0-12-812064-4.00002-5

Yang, Y., & Forsyth, D. W. (2003). Improving epicentral and magnitude estimation of earthquakes from T phases by considering the excitation function. *Bulletin of the Seismological Society of America*, *93*(5), 2106–2122. https://doi.org/10.1785/0120020215